Geometric preprocessing for measurements of comet 67P acquired by Rosetta's Visible and InfraRed Thermal Imaging Spectrometer, Mapping channel (VIRTIS-M)

D. Kappel, G. Arnold, G. Filacchione, F. Capaccioni, F. Tosi, S. Erard, M. Ciarniello, E. d'Aversa, A. Raponi, C. Leyrat, et al.

RESEARCH ARTICLE | DECEMBER 03 2024

Geometric preprocessing for measurements of comet 67P acquired by Rosetta's Visible and InfraRed Thermal Imaging Spectrometer, Mapping channel (VIRTIS-M)

D. Kappel ; G. Arnold ; G. Filacchione ; F. Capaccioni ; F. Tosi ; S. Erard ; M. Ciarniello ; E. D'Aversa ; A. Raponi ; C. Leyrat ; L. V. Moroz

Rev. Sci. Instrum. 95, 125105 (2024)
https://doi.org/10.1063/5.0226387

Review of Scientific Instruments ARTICLE pubs.aip.org/aip/rsi

Geometric preprocessing for measurements of comet 67P acquired by Rosetta's Visible and InfraRed Thermal Imaging Spectrometer, Mapping channel (VIRTIS-M)

Cite as: Rev. Sci. Instrum. 95, 125105 (2024); doi: 10.1063/5.0226387
Submitted: 1 July 2024 • Accepted: 7 November 2024 •
Published Online: 3 December 2024

D. Kappel,[1,a] G. Arnold,[2,b] G. Filacchione,[3] F. Capaccioni,[3] F. Tosi,[3] S. Erard,[4] M. Ciarniello,[3] E. D'Aversa,[3] A. Raponi,[3] C. Leyrat,[4] and L. V. Moroz[2]

AFFILIATIONS

[1] Institute of Physics and Astronomy, University of Potsdam, Karl-Liebknecht-Str. 24/25, 14476 Potsdam, Germany
[2] Institute of Planetary Research, German Aerospace Center (DLR), Rutherfordstr. 2, 12489 Berlin, Germany
[3] INAF-IAPS, Istituto di Astrofisica e Planetologia Spaziali, Via del Fosso del Cavaliere, 100, 00133 Rome, Italy
[4] LESIA, Observatoire de Paris, Université PSL, CNRS, Sorbonne Université, Université de Paris, 5 Place Jules Janssen, 92195 Meudon, France

[a] **Author to whom correspondence should be addressed:** david.kappel@alumni.uni-potsdam.de.
Also at: Institute of Planetary Research, German Aerospace Center (DLR), Rutherfordstr. 2, 12489 Berlin, Germany.
[b] **Also at:** Institute of Geoscience, University of Potsdam, Karl-Liebknecht-Str. 24/25, 14476 Potsdam, Germany.

ABSTRACT

Comet 67P/Churyumov–Gerasimenko (hereafter 67P) was the primary target of ESA's Rosetta mission. Hyperspectral images acquired by the Mapping channel of the Visible and InfraRed Thermal Imaging Spectrometer aboard Rosetta can be used to derive physical and compositional surface properties by detailed spectrophotometric analyses. This calls for a precise spatial co-registration between measurements and geometry information. In this work, we improve the wavelength-dependent co-registration and also the spatial consistency of the radiometric calibration. This is accomplished by applying a feature-based image matching method comparing measured 67P nucleus images from the entire mission to corresponding photometric simulations. The derived geometric distortions suggest previously unaccounted optical aberrations of the instrument, in conjunction with non-systematic spacecraft pointing and perspective errors, and discrepancies between the true nucleus shape at data acquisition time and the used digital shape model.

NOMENCLATURE

DSM	digital shape model
FOV	field of view
FWHM	full width at half maximum
IFOV	instantaneous FOV (FOV of a pixel)
ITF	instrument transfer function
OSF	order sorting filter
PSF	point spread function
RFM	residual feature mismatch
SC	spectral channel
SNR	signal-to-noise ratio

I. INTRODUCTION

The primary objectives of the Visible and InfraRed Thermal Imaging Spectrometer (VIRTIS, Coradini *et al.*, 2007) aboard Rosetta were the derivation of the composition and the surface properties (particle size, roughness, temperature, etc.) of the nucleus of comet 67P, the primary target of ESA's cornerstone mission

Rosetta (Glassmeier *et al.*, 2007). One of the two channels of the VIRTIS experiment, the Mapper (VIRTIS-M), had the task of producing hyperspectral images of the nucleus surface. In this paper, we provide a refinement of the VIRTIS-M data calibration and preprocessing for future refined derivations of surface properties through detailed spectrophotometric modeling.

The link between surface properties and radiance spectra can be provided by radiative transfer models like those of Hapke (Hapke, 2012) or Shkuratov (Shkuratov *et al.*, 2011) that can be used to distinguish between textural and compositional causes of spectral variability. For a reliable modeling of surface spectra, accurate information on illumination and observation geometry are required and, therefore, an exact geometric match of measured VIRTIS-M images and simulated ones. For 67P, this is particularly challenging because the nucleus is bilobate and irregularly shaped and shows a complex surface morphology. Even for the relatively small 67P nucleus ($4.1 \times 3.3 \times 1.8$ km^3 for the large lobe; $2.6 \times 2.3 \times 1.8$ km^3 for the small one, Sierks *et al.*, 2015), one needs millions of triangular facets to accurately represent the entire surface through a digital shape model (DSM) like the one by Preusker *et al.* (2017). Moreover, the lines in the VIRTIS-M images are collected at different times while scanning the scene by an internal mirror. A line is typically acquired every 20 s; hence, one has to take into account geometric changes of the scene due to both Rosetta's movement and the comet rotation.

Even without employing any simulations, pixel-level changes with wavelength of the geometric alignment of topographic features can be verified by comparing images of a given VIRTIS-M measurement at different wavelengths. Detailed comparisons between the measured images and standard pipeline geometry simulations reveal wavelength-dependent locally varying spatial mismatches of up to a few pixels. This is significant considering the moderate spatial resolution of VIRTIS-M images (IFOV = 0.25×0.25 mrad^2, i.e., 25 m surface sampling from distances of typically 100 km, with images of 256 pixels in one of the spatial dimensions, Coradini *et al.*, 2007), and the rugged topography of the comet's nucleus that leads to a dense and ever-changing distribution of light–shadow boundaries on the surface. As we will see (Sec. III), these geometric mismatches can be traced back to geometric distortions induced by the instrument's hardware setup and to an insufficient knowledge of shape and alignment of the comet nucleus and the instrument's line of sight.

It is challenging to precisely calibrate this complex instrument (Filacchione, 2006; Ammannito *et al.*, 2006; Filacchione *et al.*, 2006; and Raponi *et al.*, 2020) and, in addition, mechanical and thermal stresses during the launch, cruise, and flyby phases of the mission could have affected the geometric registration and the radiometric calibration derived on ground, which may not any more accurately represent the state of the instrument during the measurements. In the present work, we improve the geometric match, obtaining at the same time wavelength-dependent correction factors that improve the spatial consistency of the radiometric calibration (flat-field refinement).

VIRTIS-M covered a wide spectral range from the UV to the near-infrared (VIS channel: 0.22–1.05 μm, IR channel: 0.95–5.1 μm, Coradini *et al.*, 2007). At each exposure, a frame (spectrally resolved spatial line) of 432 spectral channels (or spectral bands or effective wavelengths, abbreviated as SCs) times 256 spatial pixels ("samples") was recorded by the VIS or IR detector, respectively. Data cubes were constructed by scanning the scene with a movable mirror at steps of 1 IFOV (one- vs two-dimensional IFOV is used synonymously in the following). We note that the only instantaneous information (order of seconds) in a cube is for the single acquisitions, while a full cube was typically acquired over tens of minutes. There were 257 possible mirror angles (from −32 to 32 mrad), but for most cubes, only part of this range was used. The full range of mirror angles corresponds to the range of "scanning mirror positions" from −128 to 128. The scanning of a cube could start in a forward or backward direction, and at any given scanning mirror position, which then corresponded to line 1 of this cube. Data acquired without moving the mirror resulted in pushbroom cubes. A cube can also be regarded as a collection of (non-instantaneous) "images" at different SCs, and the spectrum associated with a given pixel can consist of a collection of "spectels" defined at single given SCs. The IR channel detector was equipped with several spectral order sorting filters (OSFs) necessary to suppress the contributions from high orders of the grating. The spectral transitions between these filters were located at about SCs 43–64, 149–169, 204–217, 284–297, 351–363 (counting from SC 1), which corresponds to 1.40–1.59, 2.40–2.59, 2.92–3.04, 3.67–3.79, 4.30–4.42 μm; in the VIS there is a transition at SCs 221–223 corresponding to 0.646–0.649 μm. These OSF transitions introduced different kinds of artifacts in the affected spectral ranges, some of which will be discussed below. A cryocooler failure of the IR channel of VIRTIS-M in early May 2015 prevented the subsequent acquisition of useable IR cubes such that significantly more VIS than IR cubes are available and, for instance, no IR cubes are available at the comet's perihelion (1.24 au, 13 August 2015). We note that IR observations have been performed until the end of the mission by the spectrally high-resolution channel of the instrument (VIRTIS-H), even if without imaging capabilities.

Filacchione (2006) reported the processing of measurements performed to derive the VIRTIS-M detector responsivity and the geometric registration. This includes measurements of location as well as the shape and width of the spatial point-spread-function (PSF) for a representative selection of spectels at different wavelengths (Ammannito *et al.*, 2006; Filacchione *et al.*, 2006). Using these data, for instance, a spectral tilt in the VIS channel has been characterized. It was caused by a slight rotation of the VIS grating grooves with respect to the IR grating grooves (both gratings were integrated on the same convex optical element) and is already corrected in the standard calibration pipeline. Moreover, there is a general, constant offset of 4.11 samples between VIS and IR cubes caused by slightly different alignments of the VIS and IR detectors. We note that the PSF of the IR channel is wider than that of the VIS channel by construction because of the much faster aperture of the optics (f-number for IR: 3.2, VIS: 5.6, Coradini *et al.*, 2007) and the obstructed pupil. A number of in-flight calibration refinements (Filacchione, 2006; Raponi *et al.*, 2020) improved certain aspects of the calibration, some of which in addition changed over the course of the mission. For example, in the IR, a crack appeared affecting about half the spatial width of one of the OSFs stacked above the detector in a narrow range of SCs corresponding to the spectral range around 2.8 μm (Filacchione, 2006, Fig. 5.10). It developed early in the mission, possibly caused by vibrations during launch or thermal stresses during the detector cooldown process. Now, with the mission completed and a wealth of data available,

Raponi *et al.* (2020) systematically analyzed the IR absolute radiometric calibration in dependence on wavelength and were able to significantly improve it based on comparisons to VIRTIS-M observations of asteroid Lutetia and stars. Kappel *et al.* (2024) derived and applied a correction of the VIRTIS-M-VIS detector responsivity such that the corrected radiance spectra are not dependent on the VIS detector temperature anymore. We take the measured radiance cubes in this calibration state as the starting point ("base pipeline calibrated cubes").

In the present work, we further refine some aspects of the instrument's calibration and preprocessing. Section II details our approach to improve the geometric registration and the flat-field. In Sec. III, the results are discussed and conclusions drawn before giving a summary in Sec. IV. For better readability, some details are outsourced to the Appendix (see supplementary material).

II. GEOMETRIC DISTORTION CORRECTION

This section presents our new geometric distortion correction pipeline. First, we apply a preprocessing to the base pipeline calibrated measured radiance cubes. This includes the identification of systematic defects of the spectels on the detector (unreliable responsivity, inert spectels) and spikes, and the replacement of the affected radiances by a suitable average of the neighboring values. We then remove wavelet compression artifacts for a number of cubes that were stored in a wavelet-compressed format for the downlink to Earth. Next, we set the radiances in and near the saturation regime of the detector to NaN (Not-a-Number, treated as missing data). Finally, a number of cubes are separated into subcubes at the lines where the scanning mirror started a new cycle or reversed the scanning direction, or where the scanning direction is reversed in pushbroom cubes. Details are given in Appendix A (supplementary material).

The resulting (sub-) cubes are then compared at each given SC to VIRTIS-M images simulated according to Sec. II A to obtain an estimate of the wavelength-dependent local spatial translations needed to match the individual measured and simulated images (Sec. II B). Next, we estimate the average optical distortion field over the cubes (Sec. II C) as well as wavelength-dependent correction factors to improve the flat-field and, therefore, the spatial consistency of the radiometric calibration (Sec. II D). After that, the flat-field refinement and the correction of the average optical distortion are applied to the measured cubes before geometrically matching them in a second pass to the simulated images (Sec. II E). Finally, we investigate potential deviations between the true time tags of the VIRTIS-M acquisitions and the time tags stored in the housekeeping data (Sec. II F). An overview of the different steps performed in this work is given in Fig. 1.

We note that the derivation of the flat-field refinement can be performed only after correcting the geometric distortions because it relies on comparisons to simulated images, which requires a good geometric match. Once derived, however, the flat-field refinement has to be applied before performing the final geometric correction. The reason is that the registration by the detector is the last step in the process of measuring the radiation (after it is collected by the telescope and processed by the optics and grating) and must, therefore, be corrected first when reconstructing the radiation as it was collected by the instrument, starting from the registered data available to us.

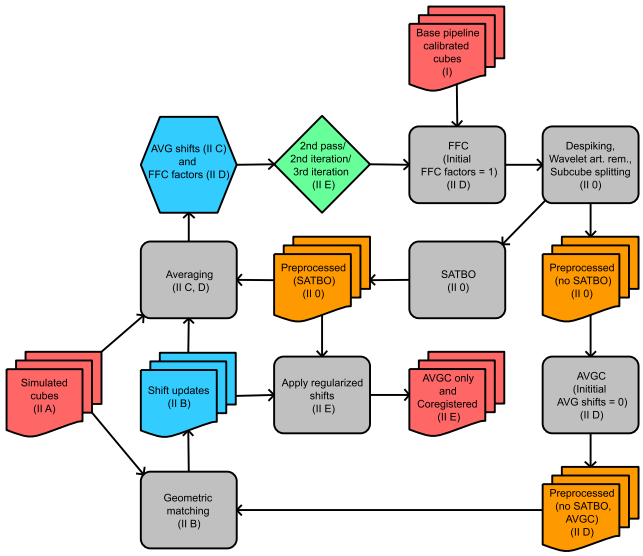

FIG. 1. Flow chart representing an overview of the different steps performed in this work. References to the respective sections are included in parentheses. Abbreviations for this chart: FFC = Flat-field correction; Wavelet art. rem. = Wavelet artifact removal; SATBO = Saturation blanking out; AVG = Average; AVGC = Average distortion correction. Background colors: red = initial datasets (here starts the flow chart) and final datasets (computed after final iteration); orange = intermediate datasets; blue = data needed for calibration; gray = applied steps; green = start of the next iteration using AVG shifts and FFC factors from previous iteration. (II 0) indicates the part of Sec. II before Sec. II A. (I) and (II 0) are improvements to the base pipeline calibration; the other steps are new.

A. Geometric modeling

An accurate spectrophotometric analysis of the VIRTIS-M measurements of the 67P nucleus surface calls for precise geometry information, in particular for solar incidence angles, observation (or emission) angles, and phase angles at the intersections of the respective viewing rays from the instrument pixels with the nucleus surface, in addition to the shadowing conditions occurring on the observed location.

We compute these data using the SPICE toolkit (Acton, 1996; Acton *et al.*, 2018), version N66, and the necessary navigational databases (SPICE kernels) for the Rosetta mission, meta-kernel v3.5.0 (ESA, 2022), as well as an accurate high-resolution digital shape model (DSM) (Preusker *et al.*, 2017). We note that, in contrast to the SPICE kernels for 67P orbit and attitude and spacecraft orbit, there are no fully reconstructed spacecraft attitude SPICE kernels (CK) for Rosetta but only the predicted ones that were commanded to the spacecraft and turned out to be sufficiently accurate to meet the requirements for VIRTIS-M (deviations corresponding to a few pixels). The DSM approximates the nucleus' geometrical shape by a polyhedron built of many triangles, called facets. Incidence, observation, and phase angle are defined with respect to the local surface normal to the sounded facet, and a viewing ray footprint is flagged as shadowed if the ray from there to the Sun (treated as a point source)

intersects the DSM again. The cited DSM consists of 44×10^6 facets with a horizontal sampling of 1–1.5 m and a typical vertical accuracy at the decimeter scale. We utilize this DSM for the geometric modeling required for the investigation and correction of the geometric distortion of the VIRTIS-M cubes.

While the physical modeling is meant to use, e.g., the Hapke (Hapke, 2012) or Shkuratov (Shkuratov *et al.*, 2011) photometric models with physical and compositional properties that are always constant on a given DSM facet but can differ between the facets, the following purely geometric analysis takes the facets to all have the same properties and bases on the parameterless Akimov disk function (Shkuratov *et al.*, 2011). The latter only depends on incidence, observation, and phase angle and is constructed to describe the topography-dependent photometric behavior of an utterly rough surface. It is computationally quite inexpensive, yet it can well describe the photometry of atmosphereless small bodies (Schröder *et al.*, 2013; Longobardo *et al.*, 2014; and 2017) and icy satellite surfaces (Filacchione *et al.*, 2022) and is actually one of the cornerstones of the Shkuratov model (Shkuratov *et al.*, 2011).

We intend to capture the effect of shape model variations inside the single pixels' footprints and to enable a flexible investigation of the spatial VIRTIS-M instrumental point spread function (PSF). For this purpose, we sample each pixel's nominal field-of-view (IFOV) plus a certain neighborhood by a dense grid of viewing rays. We want to allow for the investigation of a full width at half maximum (FWHM) of the PSF of up to 3 IFOVs (taking into account a certain neighborhood reaching beyond the nominal FWHM) and potential shifts of the real PSF center relative to the nominal center by a couple of IFOVs. Therefore, we sample for each pixel a 2D-viewing angle neighborhood corresponding to 9×9 times its nominal IFOV with a density of 7×7 viewing rays per IFOV, i.e., we consider 3969 viewing rays per pixel, including its neighborhood. We note that for all pixels of a fixed VIRTIS-M-VIS line, the viewing rays are all cast at the same ephemeris time (center of exposure); hence, the considerable overlap of viewing rays between adjacent pixels of this line can be exploited to save computational resources. The same applies to VIRTIS-M-IR, but the center exposure times can differ from the VIS ones by a few seconds due to different exposure durations, necessitating the computation of separate geometry data for VIS and IR. We also note that the ephemeris times between adjacent VIRTIS-M lines typically differ by 20 s, during which the relative position (and attitude) of spacecraft, Sun, and 67P can change noticeably. This is why we have to compute the geometric data separately for each line.

A proxy for the relative spatial variation of the surface signal is obtained by applying the Akimov disk function for each viewing ray with an illuminated footprint. The result is convolved with a simple model for the PSF, a Gaussian peaking at the nominal pixel center and with a given FWHM chosen to well describe the measured images, hence not necessarily coincident with the true FWHM of a pixel. Its value also includes, among others, the defocusing due to the presence of spherical optical elements. For illustration, in Fig. 2(c), for each pixel only the nominal pixel center geometry is considered, resulting in noise due to DSM undersampling. Figure 2(d) shows a simulation using a PSF with an FWHM of 1 IFOV, which clearly yields a too sharp image when compared to the measurement [Fig. 2(a)]. The FWHM has changed between the time

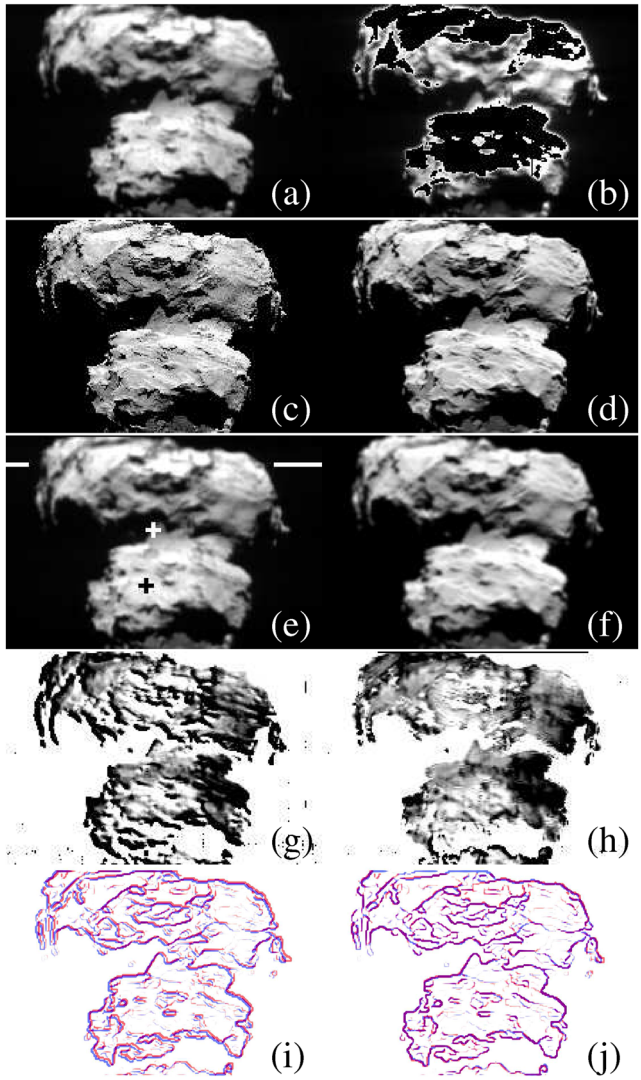

FIG. 2. Different stages of geometric preprocessing for VIRTIS-M-IR cube I1_00383489908. Spatial images are represented on a relative scale (black = low value or NaN, white = high value), vertically covering all 150 lines of this cube but horizontally clipped to the relevant spatial section. Cube acquired on February 25th, 2015, at 2.23 au heliocentric distance and 80.8 km from nucleus center. (a) Despiked, saturation-blanked-out, and flat-field-refined measured image at SC 1 (1 μm). (b) The same at SC 432 (5 μm), illustrating missing data due to detector saturation. In the following, all images refer to SC 1 (1 μm). (c) Simulated image (pixel center viewing ray only, resulting in noise due to DSM undersampling). (d) Simulated image considering PSF at FWHM of 1 IFOV. (e) Distortion-corrected measured image. (f) Simulated image at reference FWHM of 2.5 IFOV. (g) Ratio of geometrically uncorrected image a and simulated image f showing −/+15% deviations from a mean as black/white. (h) Ratio of distortion-corrected image e and simulated image (f) with the same color representation as Panel (g). (i) Edges representation (Sobel filter) of simulated image (f) (blue) and geometrically uncorrected image (a) (red). (j) Edges representation of simulated image (f) (blue) and distortion-corrected image (e) (red). White and black crosses in Panel (e) at sample/line 121/67 and 116/106, respectively, indicate footprints of spectra displayed in Fig. 8, and white horizontal lines indicate line 21, see Fig. 7.

of ground calibration (mean over all calibration measurements for VIS: 1.3 IFOV, IR: 2.2 IFOV, Filacchione, 2006, Table 4.8) and the time of 67P observations, since the measured 67P images are visually more blurry compared to the simulations using the FWHM derived during ground calibration. Therefore, we searched for the optimal FWHM value for the 67P observations by maximizing the correlation between simulated and measured images at fixed SC, for all SCs and all cubes where at least a certain number of pixels have footprints on illuminated parts of the nucleus surface. This way, we found the overall best match for a PSF with an FWHM of 2.0 IFOV in case of the VIS channel and 2.5 IFOV in case of the IR channel [e.g., Fig. 2(f)]. In the following, we will use only these values, which will turn out to be suitable for our geometric matching and enable simulations that well fit the final geometrically corrected measured images. The reasons for the FWHM change could be related to physical or alignment changes of optical parts during the launch or cruise phase of the mission.

Even though the overall appearance of the resulting synthetic VIRTIS-M images is visually similar to that of the measurements [Fig. 2(f) vs Fig. 2(a)], significant deviations of the geometric alignment at the pixel level show up. This can be highlighted by processing both the simulated and measured images with an edge-enhancing algorithm like the Sobel filter [Fig. 2(i), red and blue for measured and simulated image, respectively]. A more detailed analysis covering many VIRTIS-M cubes reveals, as we will see (Sec. II C), a spatially non-linear deviation that also varies with SC. Figure 2(j) illustrates the much better alignment achieved with the geometrically corrected measured image (result of Sec. II E). As a consequence of the geometric misalignment, the ratio [Fig. 2(g)] of the geometrically uncorrected image Fig. 2(a) and the simulated image f shows irregularities associated with the pattern of the light-shadow boundaries in the image. These irregularities virtually disappear [Fig. 2(h)] after our final correction in Sec. II E. The spatial variations in this ratio now appear physically more meaningful.

In Appendix B (supplementary material), we investigate errors of the geometric modeling.

B. Feature-based image matching

In order to obtain a first-order correction of the geometric misalignments, we apply the feature-based local image matching algorithm GeFolki (Plyer *et al.*, 2015; Brigot *et al.*, 2016). Given two images I_1 and I_2 of the same dimensions and showing approximately the same scene, this algorithm determines for each pixel $\mathbf{x}$ (vector of integer sample and line coordinate) a shift vector $\mathbf{u}(\mathbf{x})$, such that the accordingly shifted second image $I_2(\mathbf{x}+\mathbf{u}(\mathbf{x}))$ geometrically matches the first one (co-registration). The fractional values in sample and in line direction forming $\mathbf{u}(\mathbf{x})$ are determined by minimizing a cost function given by $\sum_{\mathbf{x}'\in S(\mathbf{x})}\left(I_1(\mathbf{x}')-I_2(\mathbf{x}'+\mathbf{u}(\mathbf{x}))\right)^2$, where $S(\mathbf{x})$ is a local window of size $(2r+1)\times(2r+1)$ pixels around $\mathbf{x}$, and r is a small integer. In order to also recognize larger displacements exceeding a few pixels, the images are at first down-sampled to a coarser resolution such that the largest expected displacement is just a few coarse pixels, and the corresponding cost function is minimized. The resulting coarse shift vector field is gradually refined by iterating the process for ever finer resolved images up to the actual resolution.

The application of GeFolki here yields for each measured pixel a shift vector (fractional values in sample and in line direction) that leads to an improved geometric match between the simulated image [Fig. 2(f)] and the measured one at a given SC [Fig. 2(a)], which is then shifted to obtain Fig. 2(e). This is repeated for the measured images at each SC. To improve numerical stability, radiances below a certain threshold (5% of the maximum of the smoothed image) are set to zero before applying GeFolki. In doing this, we keep a safety margin by excluding pixels from zeroing that are in a four-pixel surrounding of illuminated nucleus parts. The resulting shift vector fields are despiked and slightly smoothed, under the assumption that the true shift vector fields are not rapidly varying over the image.

Due to the feature-rich character of the 67P topography and the high quality and resolution of the shape model, this shift vector field is often quite well defined, and many cubes can be satisfactorily corrected this way. However, a local image matching algorithm always balances coarse feature resolution (with possibly suboptimal spatial matching) vs fine feature resolution (with possibly false matches). In addition, the presence of artifacts and noise, or too blurry scenes with few reference points often lead to imperfect matches. In addition, the matching stability with SC is then not always ensured, resulting in discontinuities or oscillations when visually comparing the shifted measured images cycling through the SCs or when SC-wise comparing them to the shifted measured image at a fixed SC or to the simulation. In addition, the method is not applicable to shadowed or off-nucleus pixels (e.g., coma observations), because in those cases we have no spatial reference from illuminated on-nucleus simulations.

This requires a refinement of the geometric matching strategy, which we detail in Appendix C (supplementary material), and that yields a much increased stability of the geometric matching and considerably extends the set of cubes that can be satisfactorily geometrically corrected. We also implement a regularization as part of a second pass distortion analysis (see Sec. II E), where we take into account the average geometric distortions and a corrected radiometric flat-field calibration derived from the first-pass results.

For each measured radiance cube, we finally obtain a cube of shifts in sample direction and a cube of shifts in line direction. Using these data, the unsmoothed, unnormalized, but despiked and otherwise preprocessed (see Appendix A, supplementary material) cubes are finally shifted (i.e., interpolated) to geometrically match the simulated image at each SC.

For images containing NaN values due to the presence of detector saturations, we perform the image matching for the preprocessed cubes without blanking out of saturated data, i.e., pixels affected by saturation keep their (unrealistic) nominally measured radiance value that results from the detector saturation DN level. This is because GeFolki cannot evaluate images with NaNs, and simply setting the intensities of the affected pixels to, e.g., zero would introduce abrupt spatial discontinuities (from high intensities close to saturation down to zero), leading to artifacts in the matching. Keeping the saturated values during image matching preserves the spatial continuity of the images in the spatial transition between saturated and not saturated data and, therefore, helps to avoid such artifacts. In the saturated regions themselves, the image matching yields zero shifts.

After computing the geometric corrections this way, we apply them to the images where the saturated pixels are blanked out.

We note that instead of modifying the measured data by interpolation, we could have rather shifted the simulations. However, for a given cube, this would call for SC dependent simulations. This would lead to a prohibitive amount of required storage space and processing time for the geometric modeling in the future retrieval of surface properties from the VIRTIS-M measurements. In addition, this way, it would be difficult to evaluate or even define individual spectra in cases of strong effects of the geometric distortions.

In order to minimize the loss of spatial information caused by the interpolation, we use cubic interpolation (interpolation parameter −0.5). In the vicinity of NaN-pixels, bilinear interpolation is used, though, to avoid an unnecessary spreading of the NaN-contaminated region in the image (cubic interpolation depends on a 4 × 4 pixel neighborhood, bilinear on a 2 × 2 neighborhood). Furthermore, in the bilinear interpolation domain, pixels next to an NaN-pixel are set to the average of the valid pixels of its 3 × 3 neighborhood. This way, the NaN region typically neither shrinks nor expands due to the interpolation. Pixels outside the original image are treated as NaN such that when they are shifted inside the image, the measured data are not extrapolated.

We note that the constant 4.11-sample-shift between VIS and IR cubes mentioned in Sec. I is only important when stacking corresponding VIS and IR cubes to obtain full-range spectra and will be discussed in Sec. II E. To be able to apply GeFolki, we only consider cubes with at least five spatial lines.

C. Average distortions

The sample and line shifts determined in Sec. II B are of the order of up to 4 pixels and depend on SC, sample, and scanning mirror position. In order to separate systematic from random effects, we average the shifts over many cubes as functions of SC, sample, and scanning mirror position, independently for VIS and IR cubes. For this averaging, we exclude cubes with little spatial information over the VIRTIS-M FOV (cubes with <20 lines, <25% of the pixels show illuminated nucleus parts), and pushbroom cubes (spatial scanning through variations of spacecraft position or pointing or time evolution, not by scanning mirror movements) where the geometric mismatches are possibly dominated by spacecraft position or pointing effects. We also ignore the few cubes acquired close to opposition geometry (phase angle anywhere <10°), since for them the Akimov disk function may not be a good global approximation of the spatial radiance distribution anymore. We note that in the thermal flank of the IR cubes, the Akimov disk function does not well approximate the spatial radiance distribution either, and some modeling of the thermal emission component is needed to predict the radiance image at a given wavelength, which is beyond the scope of the present work. However, for the purpose of predicting the spatial structure of the images (shapes, contours of topographical features), the Akimov disk function turns out to be still very useful except for thermal emissions in shadowed regions, but shadowed regions are excluded from the outset.

In a post-processing step, we apply a median filter (width 3 × 3) to the averaged shift cubes at the given SC and then a boxcar smoothing filter (width 3 × 3) to remove singular and high-frequency features that are not expected for the true geometric distortions. The resulting average geometric shift matrices are illustrated in Figs. 3 and 4 (actually, these images show the refined results from the second pass analysis after several iterations; see Sec. II E). The average shift in sample and line direction is (0.97, −0.02) IFOV for VIS and (1.05, −0.09) IFOV for IR, and the color bar in the figure represents deviations from these mean values. 99% of the VIS shifts in sample direction are in the interval [−1.32, 3.39] IFOV, and in line direction in [−1.49, 2.47] IFOV. In the case of IR, these intervals are [0.00, 2.92] IFOV and [−2.26, 2.36] IFOV. This demonstrates variations in the average shifts reaching 4 IFOV between low and high values. The average shift matrices clearly show systematic effects causing parts of the mismatch between simulated and uncorrected measured images. Features due to the transitions between the OSFs of the IR channel are distinctly discernible and most pronounced for the shifts in line direction (see Fig. 4). The average distortions are clearly spatially non-linear, which means that a simple pointing correction (we recall that there are no fully reconstructed spacecraft attitude SPICE kernels) or a redefinition of the VIRTIS-M-VIS and -IR FOV in the SPICE frame kernel would not resolve this issue. Moreover, the distortions are wavelength-dependent.

We investigated the reproducibility of the average shift matrices by computing them again for two disjoint subsets of the entire

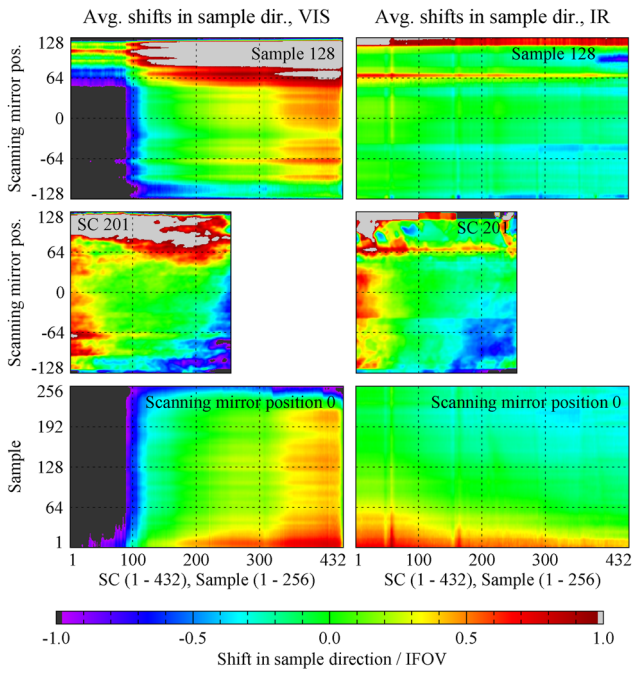

FIG. 3. Average shifts in sample direction. Panels in the left column are for VIS, and in the right column for IR. Top row panels show shift cube at sample 128 in dependence on SC and scanning mirror position; middle row shows cube at SC 201, corresponding to about 0.608 μm (VIS) or 2.88 μm (IR) in dependence on sample and scanning mirror position; bottom row shows cube at scanning mirror position 0 in dependence on SC and sample. The color bar shows values in IFOV relative to mean over the entire respective shift cube (green, colorbar value 0.0; values below −1.0 or above 1.0 are represented in black or light gray, respectively). Mean values: 0.97 IFOV (VIS), 1.05 IFOV (IR).

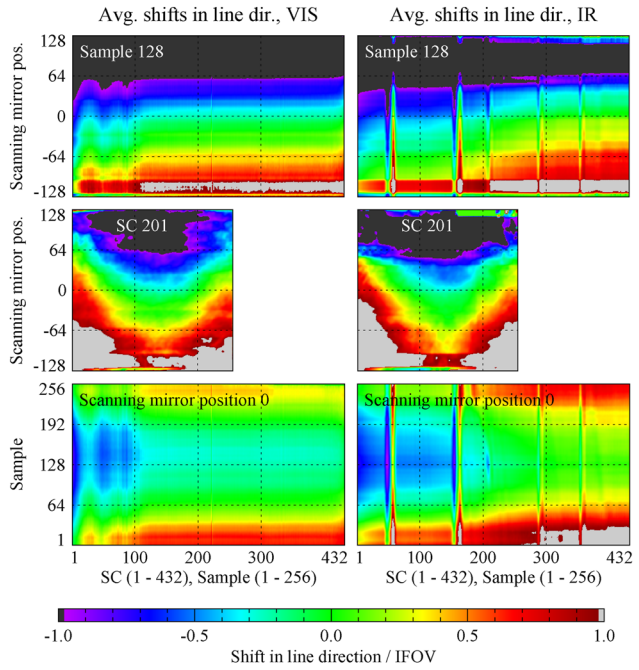

FIG. 4. Like Fig. 3, but for average shifts in line direction; mean values: −0.02 IFOV (VIS), −0.09 IFOV (IR).

database. In case of VIS, the two sets are given by the cubes where a corresponding IR cube exists (first part of the 67P data until IR cryocooler failure in May 2015, comprising 45 573 frames contributing to the averaging) and by the remaining cubes (112 458 frames). In the case of IR, we split the set of lines evenly into two chronologically consecutive parts (23 500 and 23 262 frames, respectively). The resulting shift matrices are very similar to the matrices derived from the entire database, and all qualitative features are reproduced. The typical absolute deviations over the SCs, samples, and scanning mirror positions between the VIS (IR) shift matrices for the two disjoint mission parts are 0.18 IFOV (0.19 IFOV) in sample direction and 0.13 IFOV (0.16 IFOV) in line direction. The typical absolute deviations to the matrices derived from the entire database do not exceed 0.11 IFOV.

We also investigated potential trends of the average shift matrices with mission time and instrument temperatures. For this purpose, we recalculated them while restricting ourselves to cubes acquired in certain ranges of mission time or certain ranges of instrument temperatures. However, we found no clear trends. The average shift matrices alone are not sufficient to satisfactorily correct all cubes uniformly, even considering pointing-, perspective-, 67P-rotation-model, and DSM-related deviations; also compare Sec. III C for an explanation. This does not affect our ability to perform a satisfactory distortion correction though, because we will not just use the information on the average distortions (see Sec. II E).

D. Flat-field correction

In addition to the determination of the average spatial distortions, we are now in a position to obtain a correction factor to improve the spatial consistency of the radiometric calibration, i.e., to refine the wavelength-dependent flat-field. For this purpose, we investigate the statistical bias between measured and simulated radiances directly by analyzing the responsivities of the spectels on the detector. Those are associated with the geometrically uncorrected measurements. Hence, the simulated images are shifted, using the results from Sec. II B, to geometrically match the measured ones and not the other way around. For a given cube and SC, the saturation-blanked-out measured and the simulated images are normalized to their 95th percentile to exclude effects from outliers. The resulting normalized values below 0.1 are set to NaN to exclude pixels showing only shadows or deep space, i.e., pixels with a low signal-to-noise ratio (SNR). Next, the results are again normalized to the 95th percentile, this time independently for each line, in order to discard the information on the absolute value distribution in dependence on line within a cube. Now, the ratios of the resulting normalized measured and normalized simulated lines are computed, and the median of these ratios over all lines of all considered cubes is taken (total number of frames included for VIS: 158 031, for IR: 46 762). This yields a matrix of 432 SCs × 256 samples for both the VIS and the IR channels. To just keep the information on the spatial variation discarding absolute values, we normalize these matrices for each SC. Here, the normalization factor for a given SC is the median over all samples of the matrix entries at this SC, excluding ten-pixel margins from the spatial detector edges. The ten-pixel margins are excluded because it turns out that this is where the (uncorrected) radiometric calibration is spatially least consistent, and the nucleus is often not imaged there, leading to lower statistical significance.

Assuming the errors of the simulations that are taken as references here to be random due to the diverse orientation, illumination, and observation conditions over the entire VIRTIS-M archive, the 432 × 256 VIS and IR matrices determined this way give us the statistical bias of the spatial radiometric calibration (Fig. 5). They can be regarded as flat-field refinement factors for improving the spatial consistency of the radiometric calibration and can be used to remove this bias by dividing the (geometrically uncorrected, base-pipeline-calibrated) measured cubes by them. We note that the average of the simulated images over all lines of all cubes (also normalized as described) is not constant with the spatial sample (VIS: 1% higher than average near detector center, 1% lower near detector edge; IR: 3% higher near detector center, 5% lower near detector edge). This means that taking just the average of the (normalized) measured images over all lines of all cubes as calibration refinement factors would introduce a certain observation bias, and the above-mentioned step where we divide by the normalized simulated lines is necessary to avoid this.

We also investigated the reproducibility of the bias matrices by computing them again, but for the two disjoint subsets of the entire database defined in Sec. II B, see Fig. 5, top two rows.

The VIS bias matrix exhibits a quite linear trend of decreasing values with increasing sample (order of 10% deviation between left and right spatial detector edges, Fig. 5, "VIS" panels, and Fig. 6) that is not shared by the IR matrix. On the IR channel, there appears in the short-wavelength part a gradual decrease of the values by about 4% toward the spatially outer regions of the detector (see Fig. 5, "IR mission part 1/2" panels, and Fig. 6). In the first IR mission part, another spatial trend shows up in the thermal flank that does not occur for shorter IR wavelengths (Fig. 5, "IR mission part 1") or in

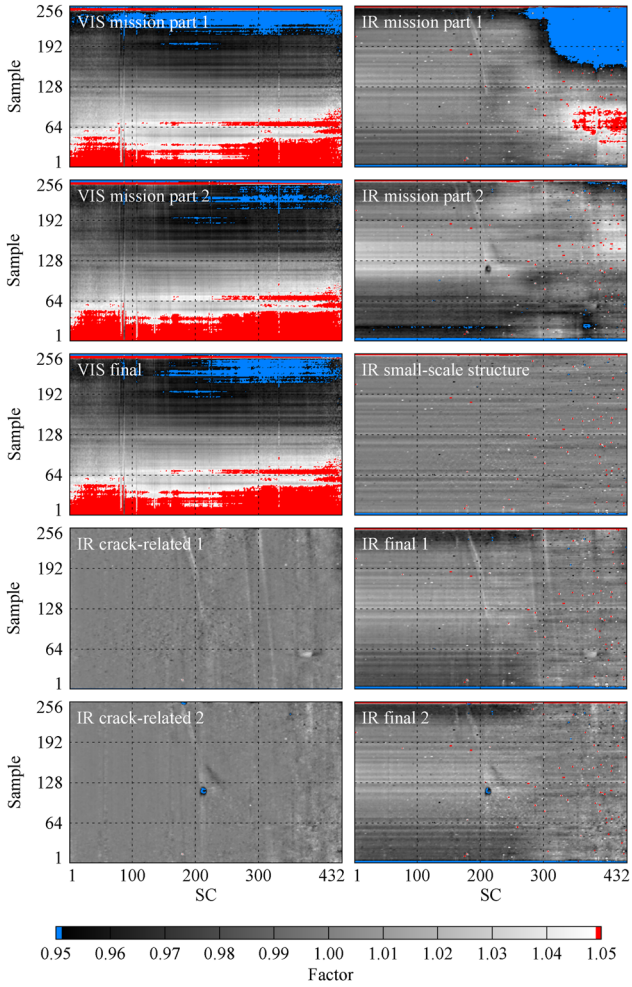

FIG. 5. Flat-field correction. Top two rows: VIS and IR bias matrices (432 SCs × 256 samples) for the first and second mission parts (differently defined for VIS and IR, see text), respectively. Panel "VIS final": VIS bias for entire VIS mission at 67P, used as VIS flat-field refinement factor. Panel "IR small-scale structure": IR bias small-scale structure matrix derived from entire IR mission. "IR crack-related 1": crack-related flat-field bias at the begin of the IR mission at 67P (Julian day 5303.3 past J2000, 2014, July 9th). "IR crack-related 2": the same at the end of the IR mission (Julian day 5572.7 past J2000, 2015, April 5th). Panels "IR final 1"/"IR final 2": regularized IR bias matrices at begin/end of IR mission, used as IR flat-field refinement factors at these mission times with time interpolation in between. Color bar values below 0.95 are represented as blue, values above 1.05 as red.

the second IR mission part. The IR matrices exhibit artifacts clearly caused by the crack in the IR OSF (Fig. 5, "IR mission part 1/2," images upper half, middle of IR spectral range). Both VIS and IR show significant deviations (up to +100% in case of VIS, ±50% in case of IR) at and close to (few pixels) the spatial detector edges (see also Fig. 6). Finally, both the VIS and IR bias matrices exhibit some irregular small-scale spatial structure (order of 1.4% magnitude in case of VIS and 1.0% in case of IR, feature widths of the order of a few samples) consistent over a wide range of SCs but not compatible between VIS and IR; also compare Fig. 6.

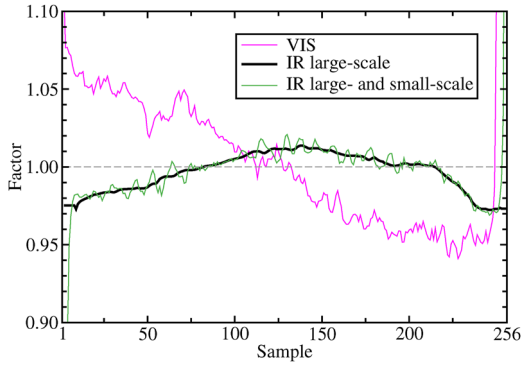

FIG. 6. Spatial profiles of flat-field correction factors. These are the medians of the (final) flat-field correction factors over the SC range 101–301 that exhibits the highest data quality in case of the VIS channel (IR: 1–251, i.e., discarding the thermal flank). "IR large- and small-scale" shows only the reproducible component for the IR channel, excluding crack-related features. In "IR large-scale," the spatially small-scale features are removed. The small-scale oscillations are not noise-related but represent the small-scale spatial structures consistent over wide spectral ranges (see Fig. 5).

We found the features of the VIS bias matrix to be largely reproducible within statistical margins. Moreover, part of the noise is reproducible and, therefore, due to some noise in the calibration base pipeline. We use the VIS bias matrix with the best SNR, i.e., the one derived from the entire mission at 67P, as a flat-field correction matrix (see Fig. 5, Panel "VIS final").

In contrast, not all features of the IR bias matrix are reproducible. We, therefore, construct the IR flat-field correction by separating reproducible from not reproducible features. This is detailed in Appendix D (supplementary material), the results of which we summarize in the present paragraph. Isolating the IR matrix artifacts related to the crack in the IR OSF, we found them to reproducibly evolve quite linearly with mission time (e.g., the small circular feature near the center of the detector in the IR matrix: degradation by 12% between the beginning of the mission at 67P and cryocooler failure). Interpolating between the regression results for the crack-related flat-field bias at the beginning and end of the IR mission at 67P (Fig. 5, Panels "IR crack-related 1," "IR crack-related 2"), we can estimate this effect for a given mission time. Next, we can separate an irregular small-scale spatial structure that is mission-time-independent and reproducible, even in the thermal flank, and consistent over wide spectral ranges in the IR matrix (VIS analogously) (see Fig. 5, Panel "IR small-scale structure," and Fig. 6). Finally, we found the spatially large-scale trend in the IR matrix (VIS analogously) to be quite consistent over the entire spectral range and reproducible, except for the IR thermal flank (Fig. 6). In case of IR, we, therefore, apply a linear cutoff between SCs 251 and 301 (3.36–3.83 μm), bridging the reproducible large-scale trend shortward of SC 251 and the constant value 1 (i.e., no spatially large-scale flat-field correction) longward of SC 301. Multiplying all three reproducible factors (mission-time-dependent crack-related features, spatially small-scale features, spatially large-scale trend with cutoff between SCs 251 and 301), we obtain a (mission-time-dependent, regularized) reproducible flat-field correction matrix for the IR data (see Fig. 5, Panels "IR final 1/2").

Furthermore, we investigated possible vignetting effects by averaging, like before, the ratios of the measured and simulated images, but this time in dependence on the scanning mirror positions. Compared to the determination of the bias matrices above, the statistics is now split into 257 scanning mirror positions and, therefore, too weak to deduce firm spatial trends with sample and scanning mirror position, and reproducibility can also not be demonstrated. Hence, we do not consider vignetting in the following. However, this analysis reveals that the spatially small-scale spatial structures of the VIS and IR bias matrices mentioned earlier are the same for all scanning mirror positions. This corroborates that they are indeed instrument transfer function (ITF)-related artifacts of the calibration base pipeline, because, if they were rather related to a bias between measurements and (imperfect) simulations, different scanning mirror positions would exhibit different such biases as different places on the nucleus surface are measured. After correcting the measured data for the small-scale features using the flat-field correction matrices, the small-scale features that were consistent for all scanning mirror positions disappear as well.

In summary, the flat-field refinement is now applied to the geometrically uncorrected, base-pipeline-calibrated cubes. After the flat-field refinement, the cubes are despiked and saturation-blanked-out (Appendix A, supplementary material) and then geometrically transformed according to the average shift matrices evaluated at the scanning mirror positions actually contributing to the respective cubes. The resulting cubes prepare the "second pass distortion analysis" presented in Sec. II E. In contrast, the basic geometrically corrected cubes (i.e., despiked, saturation-blanked-out, geometrically corrected according to Sec. II B, but without application of flat-field refinement, without consideration of average shifts from Sec. II C) used to produce the averages discussed in the present section are referred to as "first pass."

The spatial bias could potentially depend on instrument temperature and evolve with mission time, but our analysis did not show evidence for that apart from the mission time evolution of the anomalies associated with the crack in the IR OSF. We also investigated possible spatial 2D vignetting effects but found the data available for averaging to be insufficient to reliably extract spatial trends.

These kinds of moderate bias effects we are now able to correct are not unexpected for such a complex instrument as VIRTIS-M, where many aspects can only be investigated for a limited selection of samples during ground calibration and can also change over the course of such a demanding mission as Rosetta.

Figure 7 (Profiles "U" and "P") illustrates the effect of the flat-field refinement for an example spatial radiance profile of the IR cube from Fig. 2 and its corresponding VIS cube. The corrections (≤5% for VIS, ≤2% for IR over the shown sample range; larger toward the spatial detector edges, see Fig. 6) are small in absolute terms, but they are approximately consistent over all cubes, SCs, and lines and improve quantitative comparisons of radiances from different cubes sounding the same target.

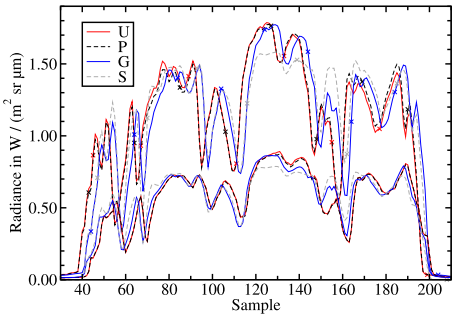

FIG. 7. Spatial radiance profiles ("U" = unpreprocessed, "P" = preprocessed, "G" = preprocessed and geometrically corrected, "S" = simulated and scaled to fit mean of Profile P) from spatial line 21 of VIRTIS-M-VIS cube V1_00383489911 (SC 201 corresponding to 0.608 μm, with symbols; constant 4.11-sample-shift between VIS and IR cubes recited in Sec. I removed in "G" and "S") and corresponding VIRTIS-M-IR cube I1_00383489908 [SC 21 corresponding to 1.19 μm, no symbols; see horizontal while indication of line 21 in Fig. 2(e)]. Only part of the sample range is displayed for better representation (outside of it, values are close to zero). Ratios between "U" and "P" are approximately given by the spatial profiles of the flat-field correction factors shown in Fig. 6.

E. Second pass distortion analysis

Now we take the obtained information on average shifts and flat-field refinement into account to refine the geometric preprocessing in a second pass. For this purpose, the preprocessed cubes with the flat-field refinements and the average shifts applied are compared to simulated images; also see the flow chart in Fig. 1.

Like in Sec. II B, GeFolki is now applied to obtain the shifts for the measurements in sample and line direction needed to geometrically match the simulations; see Appendix C (supplementary material) for details. The new shifts can be regarded as corrections to the average shifts and are non-zero because there may be random spacecraft pointing/position errors, perspective shifts with SC, or DSM inaccuracies. Since these second-pass shift corrections are typically smaller than the first-pass shifts or the average shifts, the behavior near the edges of the images, or the transition from illuminated to shadowed nucleus parts or deep-space, is better under control now and more easily regularizable. In addition, in contrast to the first pass, the flat-field refinement is now taken into account. To avoid repeated interpolation, the net shifts (average plus second-pass corrections) are then applied directly to the preprocessed measurements that have been flat-field-refined and saturation-blanked-out to yield candidates for the second-pass geometrically corrected measured cubes.

It shall be noted that, by following Appendix C (supplementary material), gaps in the reference data (shadowed regions, otherwise low-radiance regions on the nucleus, off-nucleus pixels sounding coma or deep space, even for entire off-nucleus cubes) are at least corrected using the averaged shifts plus possibly a pointing correction, which even in these cases already leads to a substantial reduction of the geometric distortions.

These candidates can sometimes suffer from geometric matching instabilities, in particular in the presence of significant noise (short- and long-wavelength flanks of VIS cubes), where the cubes have only few pixels showing illuminated nucleus parts, or when the images are blurry or exhibit few well-defined geometric features. These instabilities already occur in the first pass, but the statistical convergence leads to reasonable and useful averages. On the other hand, not applying the second-pass shift corrections but only the

averages clearly leads to stable but in many cases suboptimal corrections, e.g., with respect to spacecraft pointing/position issues or distinct residual shifts near the IR OSF transitions. This is why we use the second-pass shift corrections, but we apply a regularization to them as detailed in the following.

First, in the case of cubes with fewer than five bright pixels in the simulation (this includes cubes sounding stars or just the coma for example), we just apply the average shifts. A pixel is defined as "bright" here and in the following if the simulated intensity is ≥5% of the maximum intensity in the simulated image (and this maximum is greater than zero). Here, we refer to simulated rather than measured images because we want to include just on-nucleus pixels, and this is best determined from the simulation, thereby also avoiding possible issues with residual spikes, coma soundings, and stray light in the measured images.

Second, when there are more bright pixels, we correct for spacecraft pointing/position and DSM-related deviations by computing the medians of the second-pass shift corrections over the range of SCs 161–390 in case of VIS (because this is where the SNR is highest) and 1–300 in case of IR (because this is largely outside the thermal flank). For all SCs, this correction is then added to the average shifts. This way, the resulting images are brought to a match with the simulation, on average in the mentioned ranges. In case the wavelength dependencies of the true shifts do not deviate substantially from those of the averages, this leads to a match at all wavelengths.

The described correction corresponds to a pointing correction (spatially and spectrally constant translation resulting from median of second-pass correction over the illuminated on-nucleus pixels) and a correction of the "residual feature mismatch" (RFM). The terminology "residual" in RFM refers to the mismatch between geometrical surface features in a simulated image and a measured image after correction of the average distortions and pointing, and the RFM correction serves to minimize this mismatch. An RFM correction can refer to an individual SC or to the median RFM over a range of SCs.

We note that often an RFM is clearly discernible for close-up acquisitions of cubes where one lobe of 67P's nucleus is in the foreground with the other lobe in the background. It is often due to a perspective error, i.e., a deviation between (the time evolution of) the actual position of the spacecraft in the 67P body-fixed frame and the information thereof implied by the SPICE kernels. Naturally, a better approach than to shift the measured pixels would be to rather correct (i.e., retrieve) spacecraft position and attitude (and their time evolution over the cube) in the 67P body-fixed frame, but from a few tests we found that this does not work well based on just the VIRTIS-M measurements. In addition, 67P rotation model and DSM mismatches would not even then be corrected. The next best approach seems to be the described 2D co-registration. Incidence and observation angles may be offset from the true values this way, but only slightly (corresponding to perspective, rotation model, and DSM errors), because at least the assignments to the footprints are correct.

Third, for cubes with more than 150 bright pixels in the simulation, we have more spatial information available. We, therefore, do not have to just use the median over the mentioned wide spectral range to obtain reasonable statistical stability and can additionally include wavelength-dependent corrections. This is performed by boxcar-smoothing (width 21 SCs × 9 samples × 9 lines, or less in line direction in case of cubes with fewer lines) the second-pass shift corrections minus the median RFM correction. This way, we keep variations of this term on larger scales, but small-scale fluctuations are averaged out. The smoothing in wavelength direction excludes the ranges covering the IR OSF transitions. The resulting smoothed wavelength-dependent corrections are then added to the average shifts and the RFM correction.

As an additional refinement, we carried out a second iteration to determine the shifts based on the results of the second pass distortion analysis; also see the flow chart in Fig. 1. For this purpose, the first-iteration shifts of all cubes (the results of the present section until this point) were again averaged according to Sec. II C, and also the flat-field-correction was newly derived according to Sec. II D to obtain the first-iteration average distortions and flat-field-correction. Indeed, we found these to differ noticeably from those of the first-pass analysis. To let the geometric corrections for the off-nucleus pixels and the solar shadowed on-nucleus pixels, as well as the overall radiometric calibration benefit from the first-iteration averages, and to provide an improved initial value (the average distortions) for the geometric matching, a second iteration of the geometric matching was carried out. We also computed the average geometric distortions and flat-field corrections from the second-iteration results and judged that the deviations from the previous iteration indicated still some room for improvement. Hence, we carried out a third iteration. This time, the differences of the newly averaged geometric distortion and of the flat-field correction to those from the previous iteration turned out to be satisfactory (typical absolute deviation for flat-field correction VIS: 0.02%, IR: 0.01%, for shift in sample direction VIS: 0.04 IFOV, IR: 0.02 IFOV, for shift in line direction VIS: 0.02 IFOV, IR: 0.02 IFOV, where the largest shift differences mainly occur at the poorly covered scanning mirror positions and the noisy short- and long-wavelength flanks of the VIS cubes). We note that the just given values are not statements on the absolute accuracies of the average shift matrices and flat-field corrections, but rather on the internal consistency of the described approach to derive them.

The figures illustrating the average geometric distortions and the flat-field correction (Figs. 3–6) and all other figures in this paper in fact represent the results of this third iteration. In addition, the preprocessed and geometrically and radiometrically corrected cubes we provide (Appendix C 5, supplementary material) are the results of this last iteration.

Figure 8 illustrates characteristic effects of our corrections on radiance spectra. Overall, the spectral continuity is improved, most discernible around the IR OSF transitions and the transition between the VIS and IR spectral ranges in case of pixel footprints near a local terminator. Spectrally large-scale trends over the entire wavelength range can be affected, too. Apart from small adjustments of the absolute scaling, the flat-field correction has almost no spectrally varying effect on an individual spectrum since the correction factor is mostly constant with SC (see Fig. 5). Artifacts from saturation effects in the IR thermal flank are blanked out by NaN. Effects on example spatial radiance profiles are shown in Fig. 7. A significant improvement in the co-registration can be discerned. The flat-field correction is most pronounced in spatially outer regions of the detector, and in

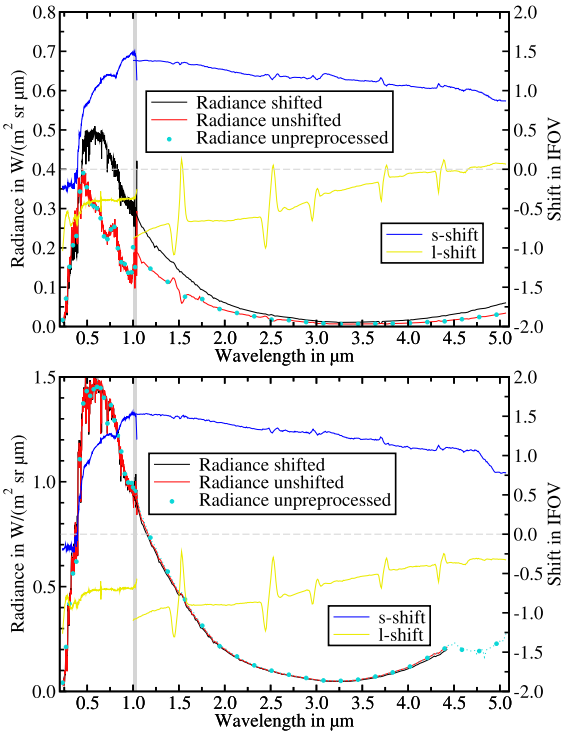

FIG. 8. Typical effects of geometric preprocessing on radiance spectra recorded in VIRTIS-M-IR cube I1_00383489908 and corresponding VIS cube V1_00383489911. Top: spectrum for sample/line = 121/67 indicated by the white cross in Fig. 2(e) close to a local terminator. Bottom: the same for sample/line = 116/106 [black cross in Fig. 2(e)] far from a local terminator. The shaded wavelength range indicates the spectral overlap between the VIS and IR channel ranges. "Radiance shifted" corresponds to Fig. 2(e), "Radiance unshifted" to Fig. 2(a), and "Radiance unpreprocessed" to base pipeline calibrated data illustrating spectral artifact (here bottom panel IR ≥ 4.5 µm) before blanking out of saturated data. "s-shift" is the spectrum of the shift in sample direction for the respective pixel, and "l-shift" is the one for line direction, both from Sec. II E results (average shift plus regularized second pass correction). The 4.11-sample-shift between VIS and IR cube is not represented in "s-shift" to omit the large offset. The VIS spectra refer to positions shifted by 4 samples (4.11 samples in case of "Radiance shifted") to make them better comparable to the IR spectra.

the case of IR, also near the central region of the detector; compare also Fig. 6.

We point out that the resulting cubes are spatially co-registered among the SCs and with respect to the simulations. In contrast, when only the average distortions are corrected, the cubes are not necessarily co-registered, but the optical distortions of the instrument are approximately corrected.

Of course, due to the complexity of the VIRTIS-M data and the many different observation situations, our distortion corrections are not optimal in each and every case, and slight residual distortions (mostly on subpixel scales) can often be noticed in direct comparisons. However, overall, the so-corrected measured cubes are both quite consistent in wavelength direction and geometrically match the simulated images well. These regularized third-iteration second-pass corrected cubes (or, short, just "second-pass corrected cubes") are the ones that we plan to use for retrieving surface information in the future.

Until now, the 4.11-sample-shift between VIS and IR data was not taken into account. For each IR cube, there is also a corresponding VIS cube (but not the other way around). For convenience, we also generate corrected VIS cubes with an additional shift of 4.11 samples (applied together with the other shifts in the final interpolation) when a corresponding IR cube exists, to optionally have a common geometric reference for VIS and IR cubes. Then, VIS and IR cubes need just be stacked to get corrected VIS–IR cubes covering the entire VIRTIS-M spectral range, but it has to be kept in mind that the PSF is wider in the IR part than in the VIS. In a future retrieval of facet properties, the VIS and IR measurements can be referred to the same geometry this way for cases where the error introduced by the different motion blurring effects (VIS typical integration time 16 s, IR 3 s) is acceptable.

F. Investigation of time tag deviations

Based on a selection of cubes from different phases of the mission at 67P, where the simulated images are very sensitive to small variations of the spacecraft position in the 67P body-fixed frame (e.g., a feature in the background lobe of the nucleus disappears or appears behind the current horizon of the foreground lobe), we investigated whether a small offset in the time tag of the acquisition of the VIRTIS-M cube can improve the geometric match between measurement (at a reference SC) and simulation. We found that offsets exceeding ±30 s can be excluded and mostly also offsets exceeding ±10 s, compared to the typical time of 20 s between the acquisitions of the single lines. In no instance did we find evidence that a time tag shift can improve the geometric match. Over such short time spans, shadow lines do not move perceptibly at the spatial resolution in the selected cubes. This means that a time tag offset is unlikely to explain why for a number of those cubes the shadow lines are perceptibly shifted with respect to the topographic features when comparing measurements and nominal simulations. The blurring of the shadow lines caused by the Sun being an extended light source, which we did not take into account in our simulations, is on a much smaller spatial scale than the observed discrepancies.

III. DISCUSSION AND CONCLUSIONS

The geometric distortions derived in Sec. II are not completely random but exhibit consistent trends with an additional seemingly random component. We interpret the behavior to be mainly caused by two different superimposing effects: the optical distortion error, which we discuss in Sec. III A, and pointing, perspective, and other errors, to be discussed in Sec. III B. We then take a closer look at causes of wavelength-dependent mismatches between simulations and measurements corrected for average distortions and pointing (Sec. III C) and characterize cubes that are difficult to match (Sec. III D). Finally, we focus on the typical impacts of our corrections on the measured spectra (Sec. III E).

A. Optical distortion error

The average of the shifts over many cubes, assuming cube-by-cube deviations from this average to be random, shows a consistent component. Some aspects of it are different between VIS and IR

(in the spectral direction and probably more related to the IR OSFs' properties; see Figs. 3 and 4, top and bottom rows); others are similar (in the spatial directions and probably more related to aberrations of the optics that is shared by the VIS and IR channels; see Figs. 3 and 4, middle rows). This leads us to the interpretation that there are previously unaccounted distortions of the instrument's optical properties. As a shorthand, we will call this "optical distortion error." We approximate it by the average shifts (Sec. II C), which we also denote by "average distortions." We note that they are spatially non-linear, since pure (spatially constant) translations in sample and line directions cannot capture their behavior.

The optical distortion error is in part a consequence of the astigmatism caused by the spherical mirrors (Piccioni *et al.*, 2007) employed in the design of the VIRTIS instrument. Because of this aberration, the best spatial and spectral focal points are located in two different positions. VIRTIS has been aligned in a configuration between these positions to guarantee the overall requirements, and the resulting spectral-spatial optical distortions are due to this compromise. The overall behavior of both the VIS and the IR shifts in the spatial directions is reminiscent of the smile and keystone optical distortions that are characteristic aberrations of hyperspectral imaging data due to lenses with spherical surfaces and with tilted optical paths (Khurshid *et al.*, 2006; Yokoya *et al.*, 2010), such as it is the case with VIRTIS-M. Differences between the SC-dependencies of the VIS and IR shifts include the anomalies occurring at OSF transitions. The OSFs are placed before the detector. Therefore, the optical beam is passing through them when it is not yet focused. This gives rise to several kinds of anomalies related to the OSF transitions, like the IR channel shift anomalies and an asymmetric behavior of the measured radiance signal at sharp features like shadow boundaries or the limb. The corresponding geometric mismatches can often not be fully corrected.

Since the scanning mirror is flat and placed in front of the telescope, it is technically not possible that the optical distortions change with scanning mirror position. However, the derived average distortions change with it, and quite linearly so, with very nearly the same slope for any given SC and sample and both in case of the VIS and the IR channel (slope −0.0106 IFOV per line, from the Theil-Sen-Siegel estimator, Siegel, 1982, which is based on repeated medians to estimate slopes and is still statistically robust even when nearly half of the data are outliers). This can be reconciled by a slight redefinition of the FOV (1.07% wider scanning angle steps counting from scanning mirror position 0), which removes the change of the optical distortions with scanning mirror position apart from noise and artifacts. At this opportunity, one can derive a redefinition of the FOV that captures the linear components of the average distortion matrices. This is achieved through a FOV that, compared to the one defined in the VIRTIS frame SPICE kernel, is 0.25% wider in sample direction counting from mid FOV and translated by 1.04 IFOV in sample direction and by −0.075 IFOV in line direction. Then the only average distortions left, apart from noise and artifacts, are those in dependence on SC and sample. They are visually very similar to the bottom panels of Figs. 3 and 4 and not represented here. The match between measured and synthetic images using a recomputed geometry based on this redefined FOV is improved, but significant mismatches remain since the SC-dependent non-linear components are not considered. In addition, the non-systematic mismatches remain. Therefore, we do not further pursue this FOV redefinition, which is mainly interpretative.

B. Pointing and perspective errors and errors related to rotation model and DSM

We now focus on the non-systematic component of the geometric mismatch between measured and simulated images. There may be mismatches between the actual relative position and pointing of the instrument in the 67P body-fixed coordinate frame and its representation in the SPICE kernels, for instance, due to real deviations or due to a low time sampling rate of actual attitude data measured for the spacecraft. In addition, we recall that there are no fully reconstructed spacecraft attitude SPICE kernels.

For pointing-related mismatches like homogeneous translations of an image in sample and line directions and rotations, we will use the shorthand "pointing error." "Perspective errors," on the other hand, are due to errors in Rosetta's position in the 67P body-fixed frame and, therefore, the observation point. They lead to perspective mismatches, which often have more subtle effects depending on the local topography and are most easily recognized when one lobe of 67P is in the foreground with the other lobe in the background. Since the VIRTIS-M image acquisition is not instantaneous, the pointing and perspective errors, which are mostly between zero and up to a few pixels, depend on the time evolution of pointing and position. This can also explain certain kinds of geometric mismatches that are of second order and much harder to recognize and correct.

Together, pointing and perspective errors contribute to the non-systematic component of the geometric mismatch, but they cannot explain all of it. Deviations between the true shape of the 67P nucleus at the time of acquisition of a cube and the DSM (Preusker *et al.*, 2017) used to compute the corresponding simulated image, most likely in the cm to m scale, can also contribute to the geometric mismatches. Such deviations can be due to the topographic evolution of surface features with mission time (boulders, cliffs, dunes, etc.) caused by cometary activity but also to (systematic or random) issues in the DSM reconstructed from images acquired by Rosetta's OSIRIS instrument (Keller *et al.*, 2007). In addition, inaccuracies in the rotation model of 67P can lead to mismatches, e.g., of shadow lines. Since we carry out the simulation in the 67P body fixed frame, the 67P rotation model is already taken into account, and errors thereof can be considered as contributors to the pointing and perspective errors. Still, the position of the Sun in the 67P body-fixed frame is affected as well, causing the mentioned mismatches not only in the shadow lines but also in the illumination angles in general. Deviations in the latter are not critical though, since the discrepancy is usually of the order of just a few degrees at most and the simulation error is continuous with illumination angle (apart from shadowing effects). Discontinuities that can occur, e.g., when the footprint of a viewing ray is due to a geometric mismatch associated with a point on the nucleus surface far away from the true one (in extreme cases on the wrong lobe), are more problematic.

A pointing error can be corrected exactly by translations and rotations of a measured image, in case the time evolution of the error over the cube acquisition is negligible. In contrast, the correction of a perspective error requires spatially non-linear shifts, in particular in the presence of a strong topographical structuring of the

observed target. In case topographical prominences cause occlusions of other parts of the nucleus, our geometric shifts cannot exactly correct perspective errors (but pointing errors), and only approximate corrections are achievable. This also applies to DSM mismatches and shadow line mismatches. The latter are mostly subpixel, but in a few cases, depending on incidence angle, observation angle, observation distance, and topographic conditions, they exceed ten pixels with respect to their topographical surroundings. They can be caused by rotation model errors as well as DSM errors of the local topography and possibly topographical prominences somewhere else.

Errors in our geometric corrections themselves mainly occur in the spectral ranges most affected by low SNR (e.g., short and long wavelength edges of the VIS cubes) and also in the ranges affected by the IR OSF transitions and the crack. Using the methods detailed in Appendix C (supplementary material, in particular matching for median images of chunks of SCs, Appendix C 1) and the regularization of the shifts (Sec. II E), we were mostly able to keep the impact of low SNR on acceptable (subpixel) levels.

C. Wavelength-dependency of perspective mismatches

After correction of the average distortions and pointing, we found the perspective errors to depend on SC. This is most evident in the IR OSF transitions when cycling through visualizations at different SCs. Other spectral ranges are affected as well, and the magnitude of this effect varies with spatial sample and scanning mirror position. This is even the case when the cubes are in addition median-RFM-corrected (Sec. II E). This is equivalent to the effect that the deviations of the full (regularized) shifts from the average shifts depend on SC, where these deviations change from cube to cube.

One possible explanation is that the geometric shifts could potentially depend on instrument temperature and evolve with mission time such that the average shifts alone cannot fully parameterize the distortions for a given cube. However, we found no clear evidence for such trends (Sec. II C). Nevertheless, even without being able to completely predict the shifts for a given cube in such a way, we can still satisfactorily correct most cubes using the individual (regularized) geometric shift cubes and not just the averaged shifts.

To provide another explanation for this behavior, we observe that the aberrations of the VIRTIS-M optics can lead to deviations of the footprint of the slit on the 67P nucleus surface from the nominal (idealized) one. This deviation depends not only on spatial sample and scanning mirror position but, possibly due to astigmatism, also on SC. In addition, there are the shift anomalies in the IR OSF transitions. In addition, we note that for a line scanner such as VIRTIS-M, the perspective from which a scene is observed naturally changes from line to line within a cube due to spacecraft motion in the body-fixed frame.

We now consider a situation where the average shift in line direction at a given SC, spatial sample, and scanning mirror position is +1 IFOV and the scanning mirror steps between consecutive acquisitions are likewise +1 IFOV. Then the true footprint is 1 IFOV behind in the scanning direction of the instrument (behind, because this needs +1 IFOV to correct it to the nominal viewing direction). Only for the acquisition at the next scanning mirror position $l_0 + 1$, the true footprint coincides with the nominal footprint at acquisition l_0. However, at $l_0 + 1$, for typical cubes acquired 20 s later than l_0, the perspective from which this footprint is observed is already slightly different from the perspective at l_0 due to spacecraft motion in the 67P body-fixed frame. The correction of the average distortion in the measured image shifts the footprint at $l_0 + 1$ into the nominal line l_0 of the corrected image to match the observed footprint to the nominal one. Hence, line l_0 of the corrected image shows footprints that are nominally aligned but observed from different perspectives after correction because the average distortion varies across the line. In the same way, the optical distortion anomalies in the IR OSF transitions cause perspective mismatches in the continuity of the measured radiances in the SC direction that concentrate in narrow SC ranges.

There are two straightforward ways to handle the optical distortions. First, the (geometrically uncorrected) measured cubes are accepted as they are, and the geometry is computed with the optical distortion taken into account. This approach requires geometry data that depend on SC. Indeed, we have computed such geometry data for selected cubes, utilizing the average distortions. The corresponding Akimov-simulations then closely follow the behavior of the measured cubes regarding, e.g., footprint deviation from nominal and perspective continuity along the SC direction. Still, mismatches related to the 67P DSM and rotation model remain, and also mismatches caused by the difference between (the time evolution of) the true pointing and position of Rosetta in the 67P body-fixed frame and those used in the simulations. In order to achieve a better match between simulation and measurement, either the simulations have to take this into account or the measurements have to be shifted accordingly. As mentioned earlier, this approach would lead either way to a large amount of required storage space and processing time for the geometric modeling in the future retrieval of surface properties from the VIRTIS-M measurements. In addition, it would be difficult to specify well-defined individual spectra because an uncorrected measured spectrum at a given sample and line results from a mix of different surface footprints.

The other way to geometrically match measurements and simulations is to shift the measurements to match the simulations. This has the disadvantage that the measurements have to be interpolated, and, as we have now seen, that the perspective after correction may not always match that of the simulation, an effect that can sometimes not be fully corrected. Mismatches related to the DSM and rotation model have to be corrected in addition either way. Balancing the disadvantages, this is the approach we have chosen to pursue in the present work.

The above proposed explanation for the failure of the average shift matrices alone to satisfactorily correct all cubes uniformly, not considering position, attitude, rotation model, and DSM issues, would explain several issues. For instance, the geometric mismatches between the measured images of a given cube at different SCs after correction of the average distortions are then really due to perspective effects that, therefore, can change from cube to cube and in different ways with SC (because the average distortions vary with SC), in a seemingly unpredictable and irreproducible way. While some cubes are extremely sensitive to perspective changes (Sec. III D), others are not or almost not. The extremely sensitive ones are nearly impossible to match, either only correcting the average distortions and pointing, or including a median RFM correction

(Sec. II E), or applying the full regularized corrections. In addition, this explains the difficulty to match the measurements in the IR OSF transitions. Moreover, the perspective mismatches are usually most pronounced near the spatial edges of a cube (for a given line, this is where the largest shifts in line direction are). Furthermore, this would explain why these perspective effects are more discernible in IR cubes than VIS cubes (because the IR OSF transitions exhibit larger shift variations in line direction and the largest VIS shift variations in line direction are in the spectral ranges strongest affected by noise and stray light masking these perspective effects; shifts in sample direction do not cause perspective mismatches).

Hence, we argue the geometric distortions of any cube and image to be largely reproducible and predictable (by taking them into account in SC-dependent geometry data) without significant effects from instrument temperature or with mission time. The complex behavior of the local perspective and inadequacies in the utilized DSM (e.g., due to topographic changes with mission time), the 67P rotational model, and Rosetta's trajectory and pointing in the 67P body-fixed frame, however, make the full exploitation of the implications impractical. The shift to a common geometry is not predictable so easy anymore and depends on cube and SC.

D. Cubes that are difficult to match

There are a number of cubes that are extremely sensitive to the tiniest perspective changes. They are incredibly difficult to match, both among the different SCs and with respect to the simulation. Most of these cubes are, at least in some of their parts, very blurry and exhibit hardly any well-defined geometrical features that can serve as references for the geometric matching. Typically, a rotation of the footprint of the slit is involved, which leads to fix points in the slit footprint over the course of a cube. Such a fix point, including a certain surrounding, appears as featureless in the measured and simulated images. Actually, we see the time development of this point over the course of the cube, a time span over which usually no recognizable changes are expected. A slight perspective change in this situation, for instance, associated with the shift anomalies in the IR OSF transitions or the crack (where the optical properties strongly change as well), leads to a large jump in the true footprint that is not reached by the regular scanning even after many frame acquisitions. Correcting this by corresponding shifts may lead to an improved alignment of the footprints, but the perspective may then be completely different from the nominal (that is, simulated) one.

Mostly our geometric matching leads to a balance between a correction of the footprint dislocation and the perspective mismatch such that neither is fully corrected but both are somewhat corrected. DSM mismatches amplify these issues. Cubes that are only moderately sensitive to perspective changes can usually be satisfactorily corrected. However, even when the geometric features are well matched in most spectral ranges, matching anomalies remain in the IR OSF transitions or in connection with the crack because perspective mismatches often cannot be well compensated.

E. Impact on measured spectra

A selection of geometrically preprocessed spectra is displayed in Fig. 8 in comparison to the corresponding unprocessed spectra. We note that in the case of the pixel footprint close to a local terminator, the artifacts at the OSF transitions of VIRTIS-M-IR can now be considerably reduced (Fig. 8, top). In the uncorrected measurements, the artifacts are caused by a number of SCs of this pixel having their actual footprints closer to the shadowed region just across the terminator, while other SCs are still fully sounding the illuminated area, a behavior that is adjusted by the geometric distortion correction. This is the reason why these kinds of artifacts occur at footprints in the vicinity of large brightness contrasts, but analogously, the spectral information is spatially mixed also in other areas, with adverse effect particularly near boundaries between areas with different surface properties, e.g., at boundaries of water ice patches or possibly of morphologic regions. Due to the complex topography and morphology of 67P, such artifact-affected pixels are quite abundant in the VIRTIS-M data. The artifacts at the OSF transitions have prevented the quantitative analysis of the respective spectral ranges (see list in Sec. II C) in earlier papers (Capaccioni *et al.*, 2015; Filacchione *et al.*, 2016b; and Raponi *et al.*, 2016). This includes one of the water ice absorption bands, i.e., the one at 1.5 μm.

The same terminator effect can be observed at the transition between the VIS and IR range and within the VIS range, as also illustrated in Fig. 8, top. Due to the change of the IR shift in line direction between 2.5 and 5.1 μm over 0.5 IFOV in this case, the overall spectral behavior can also change significantly in the long-wavelength range, affecting surface temperature retrieval. Although the latter has been performed by Tosi *et al.* (2019) utilizing only the spectral range 4.5–5.1 μm over which the spectral behavior itself is not distorted much, the precise association of the retrieved temperature data to the actual surface footprint location or to quantities retrieved from other wavelength ranges is certainly affected. This is especially relevant in the vicinity of terminators, where the calculation of spatial and temporal temperature gradients is clearly affected, with an impact on the investigation of thermal degradation of the surface material.

Even though the bottom panel of Fig. 8 depicts a spectrum far from a local terminator, the radiance trend of the thermal flank ≥3.5 μm is slightly different after correction with corresponding effect on retrieved surface temperatures. Otherwise, the geometric distortion correction does not significantly affect the spectrum shown in the bottom panel.

It shall be mentioned that there are instances where the geometric correction and flat-field refinement do not completely remove spectral artifacts (in part due to our simplified FWHM model of the PSF or residual perspective mismatches) or even introduce new issues, but for the vast majority of individual spectra, the spectral behavior is improved. It is clear that the co-registration of the measured images with the simulated ones and the co-registration among the images at different SCs are important prerequisites to the quantitative evaluation of the individual spectra.

Previous surface property analyses based on VIRTIS-M measurements are only marginally affected by this geometric mismatch because they mostly rely on statistical comparisons (e.g., for extended regions on the nucleus surface, over extended time spans) where pixel-level mismatches average out (e.g., Capaccioni *et al.*, 2015; Ciarniello *et al.*, 2015; 2016; Raponi *et al.*, 2016; Filacchione *et al.*, 2016a; and Tosi *et al.*, 2019), or no spatial information is taken into account due to global averaging (Raponi *et al.*, 2020). Mainly single-cube pixel-level analyses would potentially be affected (e.g., Filacchione *et al.*, 2016b; 2016c), but in the cited cases the measured spectra are still averaged over a number of pixels, the

geometry varies not significantly in the surroundings of the investigated targets, and the used wavelength ranges are comparatively narrow and, therefore, the measurements do not suffer a large spatial shift variation over the wavelengths. In addition, spectral albedos derived from the measured radiance spectra by a photometrical correction are affected by a geometric mismatch, but normalization at a given wavelength reduces the resulting error. The main effect in these cases is on the precise association to the geometry, i.e., longitude and latitude range or DSM facets covered by the areas of interest, and the pixel-level comparison of data from different cubes nominally showing the same footprint coordinates. The two areas of interest in (Filacchione *et al.*, 2016b) extend over the order of 100 m and were imaged by four VIRTIS-M-IR cubes at spatial resolutions of 12.5, 7.5, 2.5, and 7.5 m per pixel, respectively, with geometric mismatches at 2.0 μm of 0.9, 1.5, 4.2, and 1.7 pixels, corresponding to 11 m on average. The two areas of interest in (Filacchione *et al.*, 2016c) were sounded by two VIRTIS-M-IR cubes (a few pixels each) at 20 m per pixel with geometric mismatches at 2.0 μm of 0.8 and 1.2 pixels, respectively, corresponding to 20 m on average.

IV. SUMMARY

In the present work, we performed a geometric correction of hyperspectral images of comet 67P acquired by the VIRTIS-M instrument onboard Rosetta and derived an improvement of the radiometric flat-field calibration. We provide two different versions of corrected data, first, where only the optical distortions of the instrument are corrected, and second, where in addition geometric surface features exhibited in the measurements are aligned to the ones in the simulations (wavelength-dependent co-registration); see Appendix C 5 (supplementary material). The second version is required to compensate geometric mismatches caused by pointing and perspective errors as well as potential 67P rotation model inaccuracies and deviations between the true shape of the nucleus at acquisition time and the utilized digital shape model. The co-registration success depends on the spatial distribution of the observed surface features and the image quality. The stability of the co-registration among different SCs is now very good for most cubes.

The presented method of the geometric correction and the flat-field correction can be applied to imaging data acquired by other missions to atmosphereless solar system bodies with feature-rich topographies and a high quality DSM available.

In future retrieval of nucleus surface properties using, e.g., the Hapke or Shkuratov models, the remaining mismatches are expected to mainly have localized effects. This means that, after our corrections, the association of the measured radiance spectra to the correct surface footprints is problematic mostly only in places with strong perspective discontinuities, shifted shadow lines, and DSM errors. Errors in the associated incidence and observation angles are expected to be acceptable as long as the assignments to the footprints are correct.

The now achieved overall good match between the geometrically and flat-field corrected measurements and the geometry data taking into account the instrument's PSF enable an improved photometric analysis. Using an approach like the one by Kappel *et al.* (2025), it is possible to very efficiently perform the geometric modeling, and one can focus on spectral modeling, e.g., applying the models by Hapke (2012) or Shkuratov *et al.* (2011), possibly also including a thermal model. Based on this, we intend to retrieve compositional and physical surface properties by fitting simulated to measured spectra in our future work. Here, we will assume the facet properties to be constant over time within a certain time span where heliocentric distance change and, therefore, overall surface evolution are small. This will allow us to retrieve the facet properties as parameters that are common to multiple observations of the same target region on the nucleus, for which we intend to apply the Multi-Spectrum Retrieval algorithm (Kappel, 2014). This way, we can exploit that the photometric information is sampled by different observation and illumination geometries, resolving degeneracies of the measured spectra acquired in just a single measurement, i.e., at just one geometry. An indispensable prerequisite for this approach is the spatial and radiometric consistency of the measurements that we were able to improve in the present work.

SUPPLEMENTARY MATERIAL

In the supplementary material (Appendix), we present details on the data preprocessing, geometric modeling errors, feature-based image matching, and construction of the IR channel flat-field correction. We also provide the calibration data derived in the present work (flat-field correction factors, cubes of average shifts in sample and in line direction for both the VIS and the IR channel data, lists for separating cubes into subcubes); see description in Appendix C 5 (supplementary material).

ACKNOWLEDGMENTS

We thank the following institutions and agencies for support of this work: the Italian Space Agency (ASI, Italy, Contract No. I/024/12/1), the Centre National d'Etudes Spatiales (CNES, France), DLR (Germany), NASA (USA), and the Rosetta Program and Science and Technology Facilities Council (UK). VIRTIS was built by a consortium that includes Italy, France, and Germany, under the scientific responsibility of the Istituto di Astrofisica e Planetologia Spaziali of INAF, Italy, which also has guided the scientific operations. The VIRTIS instrument development, led by the prime contractor Leonardo-Finmeccanica (Florence, Italy), has been funded and managed by ASI, with contributions from Observatoire de-Meudon financed by CNES and from DLR. We thank the Rosetta Science Ground Segment and the Rosetta Mission Operations Centre for their support throughout all the phases of the mission. D.K. acknowledges DFG under Grant No. KA 3757/2-1.

AUTHOR DECLARATIONS

Conflict of Interest

The authors have no conflicts to disclose.

Author Contributions

D. Kappel: Conceptualization (lead); Data curation (equal); Formal analysis (lead); Funding acquisition (lead); Investigation (lead);

Methodology (lead); Software (lead); Visualization (lead); Writing – original draft (lead); Writing – review & editing (lead). **G. Arnold**: Conceptualization (equal); Project administration (equal); Resources (equal); Supervision (equal); Writing – review & editing (equal). **G. Filacchione**: Data curation (equal); Formal analysis (equal); Methodology (equal); Software (equal); Validation (equal); Writing – review & editing (equal). **F. Capaccioni**: Data curation (equal); Formal analysis (equal); Methodology (equal); Software (equal); Validation (equal); Writing – review & editing (equal). **F. Tosi**: Data curation (equal); Formal analysis (equal); Writing – review & editing (equal). **S. Erard**: Data curation (equal); Resources (equal); Software (equal); Writing – review & editing (equal). **M. Ciarniello**: Formal analysis (equal); Software (equal); Writing – review & editing (equal). **E. D'Aversa**: Formal analysis (equal); Writing – review & editing (equal). **A. Raponi**: Data curation (equal); Formal analysis (equal); Writing – review & editing (equal). **C. Leyrat**: Data curation (equal); Writing – review & editing (equal). **L. V. Moroz**: Formal analysis (equal); Writing – review & editing (equal).

DATA AVAILABILITY

The VIRTIS-M data are available at ESA's Planetary Science Archive (https://www.cosmos.esa.int/web/psa/rosetta). The preprocessed cubes, the geometrically corrected preprocessed cubes, and the simulated images, as detailed in Appendix C 5 (supplementary material), are available as a Virtual Observatory service with EPN-TAP access (vros_geocor), accessible, e.g., from the VESPA portal set up in Europlanet (https://vespa.obspm.fr).

REFERENCES

Acton, C. H., Planet. Space Sci. **44**, 65 (1996).

Acton, C., Bachman, N., Semenov, B., and Wright, E., Planet. Space Sci. **150**, 9 (2018).

Ammannito, E., Filacchione, G., Coradini, A., Capaccioni, F., Piccioni, G., de Sanctis, M. C., Dami, M., and Barbis, A., Rev. Sci. Instrum. **77**, 093109 (2006).

Brigot, G., Colin-Koeniguer, E., Plyer, A., and Janez, F., IEEE J. Sel. Top. Appl. Earth Obs. Remote Sens. **9**, 2923 (2016).

Capaccioni, F., Coradini, A., Filacchione, G., Erard, S., Arnold, G., Drossart, P., De Sanctis, M. C., Bockelee-Morvan, D., Capria, M. T., Tosi, F., Leyrat, C., Schmitt, B., Quirico, E., Cerroni, P., Mennella, V., Raponi, A., Ciarniello, M., McCord, T., Moroz, L., Palomba, E., Ammannito, E., Barucci, M. A., Bellucci, G., Benkhoff, J., Bibring, J. P., Blanco, A., Blecka, M., Carlson, R., Carsenty, U., Colangeli, L., Combes, M., Combi, M., Crovisier, J., Encrenaz, T., Federico, C., Fink, U., Fonti, S., Ip, W. H., Irwin, P., Jaumann, R., Kuehrt, E., Langevin, Y., Magni, G., Mottola, S., Orofino, V., Palumbo, P., Piccioni, G., Schade, U., Taylor, F., Tiphene, D., Tozzi, G. P., Beck, P., Biver, N., Bonal, L., Combe, J. P., Despan, D., Flamini, E., Fornasier, S., Frigeri, A., Grassi, D., Gudipati, M., Longobardo, A., Markus, K., Merlin, F., Orosei, R., Rinaldi, G., Stephan, K., Cartacci, M., Cicchetti, A., Giuppi, S., Hello, Y., Henry, F., Jacquinod, S., Noschese, R., Peter, G., Politi, R., Reess, J. M., and Semery, A., Science **347**, aaa0628 (2015).

Ciarniello, M., Capaccioni, F., Filacchione, G., Raponi, A., Tosi, F., De Sanctis, M. C., Capria, M. T., Erard, S., Bockelee-Morvan, D., Leyrat, C., Arnold, G., Barucci, A., Beck, P., Bellucci, G., Fornasier, S., Longobardo, A., Mottola, S., Palomba, E., Quirico, E., and Schmitt, B., Astron. Astrophys. **583**, A31 (2015).

Ciarniello, M., Raponi, A., Capaccioni, F., Filacchione, G., Tosi, F., De Sanctis, M. C., Kappel, D., Rousseau, B., Arnold, G., Capria, M. T., Barucci, M. A., Quirico, E., Longobardo, A., Kuehrt, E., Mottola, S., Erard, S., Bockelée-Morvan, D., Leyrat, C., Migliorini, A., Zinzi, A., Palomba, E., Schmitt, B., Piccioni, G., Cerroni, P., Ip, W. H., Rinaldi, G., and Salatti, M., Mon. Not. R. Astron. Soc. **462**, S443 (2016).

Coradini, A., Capaccioni, F., Drossart, P., Arnold, G., Ammannito, E., Angrilli, F., Barucci, A., Bellucci, G., Benkhoff, J., Bianchini, G., Bibring, J. P., Blecka, M., Bockelee-Morvan, D., Capria, M. T., Carlson, R., Carsenty, U., Cerroni, P., Colangeli, L., Combes, M., Combi, M., Crovisier, J., De Sanctis, M. C., Encrenaz, E. T., Erard, S., Federico, C., Filacchione, G., Fink, U., Fonti, S., Formisano, V., Ip, W. H., Jaumann, R., Kuehrt, E., Langevin, Y., Magni, G., McCord, T., Mennella, V., Mottola, S., Neukum, G., Palumbo, P., Piccioni, G., Rauer, H., Saggin, B., Schmitt, B., Tiphene, D., and Tozzi, G., Space Sci. Rev. **128**, 529 (2007).

ESA, Rosetta SPICE kernels set V3.5.0, 2022, last accessed January 16, 2024.

Filacchione, G., "Calibrazioni a terra e prestazioni in volo di spettrometri ad immagine nel visibile e nel vicino infrarosso per l'esplorazione planetaria," Ph.D. thesis, INAF-IASF, Rome, Italy, 2006.

Filacchione, G., Ammannito, E., Coradini, A., Capaccioni, F., Piccioni, G., de Sanctis, M. C., Dami, M., and Barbis, A., Rev. Sci. Instrum. **77**, 103106 (2006).

Filacchione, G., Capaccioni, F., Ciarniello, M., Raponi, A., Tosi, F., De Sanctis, M. C., Erard, S., Morvan, D. B., Leyrat, C., Arnold, G., Schmitt, B., Quirico, E., Piccioni, G., Migliorini, A., Capria, M. T., Palomba, E., Cerroni, P., Longobardo, A., Barucci, A., Fornasier, S., Carlson, R. W., Jaumann, R., Stephan, K., Moroz, L. V., Kappel, D., Rousseau, B., Fonti, S., Mancarella, F., Despan, D., and Faure, M., Icarus **274**, 334 (2016a).

Filacchione, G., de Sanctis, M. C., Capaccioni, F., Raponi, A., Tosi, F., Ciarniello, M., Cerroni, P., Piccioni, G., Capria, M. T., Palomba, E., Bellucci, G., Erard, S., Bockelee-Morvan, D., Leyrat, C., Arnold, G., Barucci, M. A., Fulchignoni, M., Schmitt, B., Quirico, E., Jaumann, R., Stephan, K., Longobardo, A., Mennella, V., Migliorini, A., Ammannito, E., Benkhoff, J., Bibring, J. P., Blanco, A., Blecka, M. I., Carlson, R., Carsenty, U., Colangeli, L., Combes, M., Combi, M., Crovisier, J., Drossart, P., Encrenaz, T., Federico, C., Fink, U., Fonti, S., Ip, W. H., Irwin, P., Kuehrt, E., Langevin, Y., Magni, G., McCord, T., Moroz, L., Mottola, S., Orofino, V., Schade, U., Taylor, F., Tiphene, D., Tozzi, G. P., Beck, P., Biver, N., Bonal, L., Combe, J. P., Despan, D., Flamini, E., Formisano, M., Fornasier, S., Frigeri, A., Grassi, D., Gudipati, M. S., Kappel, D., Mancarella, F., Markus, K., Merlin, F., Orosei, R., Rinaldi, G., Cartacci, M., Cicchetti, A., Giuppi, S., Hello, Y., Henry, F., Jacquinod, S., Reess, J. M., Noschese, R., Politi, R., and Peter, G., Nature **529**, 368 (2016b).

Filacchione, G., Raponi, A., Capaccioni, F., Ciarniello, M., Tosi, F., Capria, M. T., De Sanctis, M. C., Migliorini, A., Piccioni, G., Cerroni, P., Barucci, M. A., Fornasier, S., Schmitt, B., Quirico, E., Erard, S., Bockelee-Morvan, D., Leyrat, C., Arnold, G., Mennella, V., Ammannito, E., Bellucci, G., Benkhoff, J., Bibring, J. P., Blanco, A., Blecka, M. I., Carlson, R., Carsenty, U., Colangeli, L., Combes, M., Combi, M., Crovisier, J., Drossart, P., Encrenaz, T., Federico, C., Fink, U., Fonti, S., Fulchignoni, M., Ip, W. H., Irwin, P., Jaumann, R., Kuehrt, E., Langevin, Y., Magni, G., McCord, T., Moroz, L., Mottola, S., Palomba, E., Schade, U., Stephan, K., Taylor, F., Tiphene, D., Tozzi, G. P., Beck, P., Biver, N., Bonal, L., Combe, J. P., Despan, D., Flamini, E., Formisano, M., Frigeri, A., Grassi, D., Gudipati, M. S., Kappel, D., Longobardo, A., Mancarella, F., Markus, K., Merlin, F., Orosei, R., Rinaldi, G., Cartacci, M., Cicchetti, A., Hello, Y., Henry, F., Jacquinod, S., Reess, J. M., Noschese, R., Politi, R., and Peter, G., Science **354**, 1563 (2016c).

Filacchione, G., Ciarniello, M., D'Aversa, E., Capaccioni, F., Clark, R. N., Buratti, B. J., Helfenstein, P., Stephan, K., and Plainaki, C., Icarus **375**, 114803 (2022); arXiv:2111.15541 [astro-ph.EP].

Glassmeier, K.-H., Boehnhardt, H., Koschny, D., Kührt, E., and Richter, I., Space Sci. Rev. **128**, 1 (2007).

Hapke, B., *Theory of Reflectance and Emittance Spectroscopy*, 2nd ed. (Cambridge University Press, 2012).

Kappel, D., J. Quant. Spectrosc. Radiat. Transfer **133**, 153 (2014).

Kappel, D., Arnold, G., Filacchione, G., Capaccioni, F., Tosi, F., Erard, S., Ciarniello, M., D'Aversa, E., Raponi, A., Leyrat, C., and Moroz, L., Rev. Sci. Instrum. **95**, 105121 (2024).

Kappel, D., Arnold, G., Filacchione, G., Capaccioni, F., Tosi F., Erard, S., Ciarniello, M., D'Aversa, F., Raponi, A. Leyrat, C., and Moroz, L. V., "Efficient photometric simulations for the comet 67P/C-G nucleus using high-resolution and decimated digital shape models" (unpublished) (2025).

Keller, H. U., Barbieri, C., Lamy, P., Rickman, H., Rodrigo, R., Wenzel, K. P., Sierks, H., A'Hearn, M. F., Angrilli, F., Angulo, M., Bailey, M. E., Barthol, P., Barucci, M. A., Bertaux, J. L., Bianchini, G., Boit, J. L., Brown, V., Burns, J. A., Büttner, I., Castro, J. M., Cremonese, G., Curdt, W., Deppo, V. D., Debei, S., Cecco, M. D., Dohlen, K., Fornasier, S., Fulle, M., Germerott, D., Gliem, F., Guizzo, G. P., Hviid, S. F., Ip, W. H., Jorda, L., Koschny, D., Kramm, J. R., Kührt, E., Küppers, M., Lara, L. M., Llebaria, A., López, A., López-Jimenez, A., López-Moreno, J., Meller, R., Michalik, H., Michelena, M. D., Müller, R., Naletto, G., Origné, A., Parzianello, G., Pertile, M., Quintana, C., Ragazzoni, R., Ramous, P., Reiche, K. U., Reina, M., Rodríguez, J., Rousset, G., Sabau, L., Sanz, A., Sivan, J. P., Stöckner, K., Tabero, J., Telljohann, U., Thomas, N., Timon, V., Tomasch, G., Wittrock, T., and Zaccariotto, M., Space Sci. Rev. **128**, 433 (2007).

Khurshid, K. S., Staenz, K., Sun, L., Neville, R., White, H. P., Bannari, A., Champagne, C. M., Hitchcock, R., and Can, J., Can. J. Remote Sens. **32**, 84 (2006).

Longobardo, A., Palomba, E., Capaccioni, F., De Sanctis, M. C., Tosi, F., Ammannito, E., Schröder, S. E., Zambon, F., Raymond, C. A., and Russell, C. T., Icarus **240**, 20 (2014).

Longobardo, A., Palomba, E., Capaccioni, F., Ciarniello, M., Tosi, F., Mottola, S., Moroz, L., Filacchione, G., Raponi, A., Quirico, E., Zinzi, A., Capria, M. T., Bockelee-Morvan, D., Erard, S., Leyrat, C., Rinaldi, G., and Dirri, F., Mon. Not. R. Astron. Soc. **469**, S346 (2017).

Piccioni, G., Drossart, P., Suetta, E., Cosi, M., Ammannito, E., Barbis, A., Berlin, R., Boccaccini, A., Bonello, G., Bouyé, M. *et al.*, ESA Spec. Publ. **1295**, 1–27 (2007e); available at https://sci.esa.int/s/wNRbydw.

Plyer, A., Colin-Koeniguer, E., and Weissgerber, F., IEEE Geosci. Remote Sens. Lett. **12**, 2198 (2015).

Preusker, F., Scholten, F., Matz, K. D., Roatsch, T., Hviid, S. F., Mottola, S., Knollenberg, J., Kührt, E., Pajola, M., Oklay, N., Vincent, J. B., Davidsson, B., A'Hearn, M. F., Agarwal, J., Barbieri, C., Barucci, M. A., Bertaux, J. L., Bertini, I., Cremonese, G., Da Deppo, V., Debei, S., De Cecco, M., Fornasier, S., Fulle, M., Groussin, O., Gutiérrez, P. J., Güttler, C., Ip, W. H., Jorda, L., Keller, H. U., Koschny, D., Kramm, J. R., Küppers, M., Lamy, P., Lara, L. M., Lazzarin, M., Lopez Moreno, J. J., Marzari, F., Massironi, M., Naletto, G., Rickman, H., Rodrigo, R., Sierks, H., Thomas, N., and Tubiana, C., Astron. Astrophys. **607**, L1 (2017).

Raponi, A., Ciarniello, M., Capaccioni, F., Filacchione, G., Tosi, F., De Sanctis, M. C., Capria, M. T., Barucci, M. A., Longobardo, A., Palomba, E., Kappel, D., Arnold, G., Mottola, S., Rousseau, B., Quirico, E., Rinaldi, G., Erard, S., Bockelee-Morvan, D., and Leyrat, C., Mon. Not. R. Astron. Soc. **462**, S476 (2016); arXiv:1612.02231 [astro-ph.EP].

Raponi, A., Ciarniello, M., Capaccioni, F., Mennella, V., Filacchione, G., Vinogradoff, V., Poch, O., Beck, P., Quirico, E., De Sanctis, M. C., Moroz, L. V., Kappel, D., Erard, S., Bockelée-Morvan, D., Longobardo, A., Tosi, F., Palomba, E., Combe, J. P., Rousseau, B., Arnold, G., Carlson, R. W., Pommerol, A., Pilorget, C., Fornasier, S., Bellucci, G., Barucci, A., Mancarella, F., Formisano, M., Rinaldi, G., Istiqomah, I., and Leyrat, C., Nat. Astron. **4**, 500 (2020).

Schröder, S., Mottola, S., Keller, H., Raymond, C., and Russell, C., Planet. Space Sci. **85**, 198 (2013).

Shkuratov, Y., Kaydash, V., Korokhin, V., Velikodsky, Y., Opanasenko, N., and Videen, G., Planet. Space Sci. **59**, 1326 (2011).

Siegel, A. F., Biometrika **69**, 242 (1982).

Sierks, H., Barbieri, C., Lamy, P. L., Rodrigo, R., Koschny, D., Rickman, H., Keller, H. U., Agarwal, J., A'Hearn, M. F., Angrilli, F., Auger, A.-T., Barucci, M. A., Bertaux, J.-L., Bertini, I., Besse, S., Bodewits, D., Capanna, C., Cremonese, G., Da Deppo, V., Davidsson, B., Debei, S., De Cecco, M., Ferri, F., Fornasier, S., Fulle, M., Gaskell, R., Giacomini, L., Groussin, O., Gutierrez-Marques, P., Gutiérrez, P. J., Güttler, C., Hoekzema, N., Hviid, S. F., Ip, W.-H., Jorda, L., Knollenberg, J., Kovacs, G., Kramm, J. R., Kührt, E., Küppers, M., La Forgia, F., Lara, L. M., Lazzarin, M., Leyrat, C., Lopez Moreno, J. J., Magrin, S., Marchi, S., Marzari, F., Massironi, M., Michalik, H., Moissl, R., Mottola, S., Naletto, G., Oklay, N., Pajola, M., Pertile, M., Preusker, F., Sabau, L., Scholten, F., Snodgrass, C., Thomas, N., Tubiana, C., Vincent, J.-B., Wenzel, K.-P., Zaccariotto, M., and Pätzold, M., Science **347**, aaa1044 (2015).

Tosi, F., Capaccioni, F., Capria, M. T., Mottola, S., Zinzi, A., Ciarniello, M., Filacchione, G., Hofstadter, M., Fonti, S., Formisano, M., Kappel, D., Kührt, E., Leyrat, C., Vincent, J. B., Arnold, G., De Sanctis, M. C., Longobardo, A., Palomba, E., Raponi, A., Rousseau, B., Schmitt, B., Barucci, M. A., Bellucci, G., Benkhoff, J., Bockelée-Morvan, D., Cerroni, P., Combe, J. P., Despan, D., Erard, S., Mancarella, F., McCord, T. B., Migliorini, A., Orofino, V., and Piccioni, G., Nat. Astron. **3**, 649 (2019).

Yokoya, N., Miyamura, N., and Iwasaki, A., "Multispectral, hyperspectral, and ultraspectral remote sensing technology," Proc. SPIE **7857**, 78570B (2010).